CHALMERS

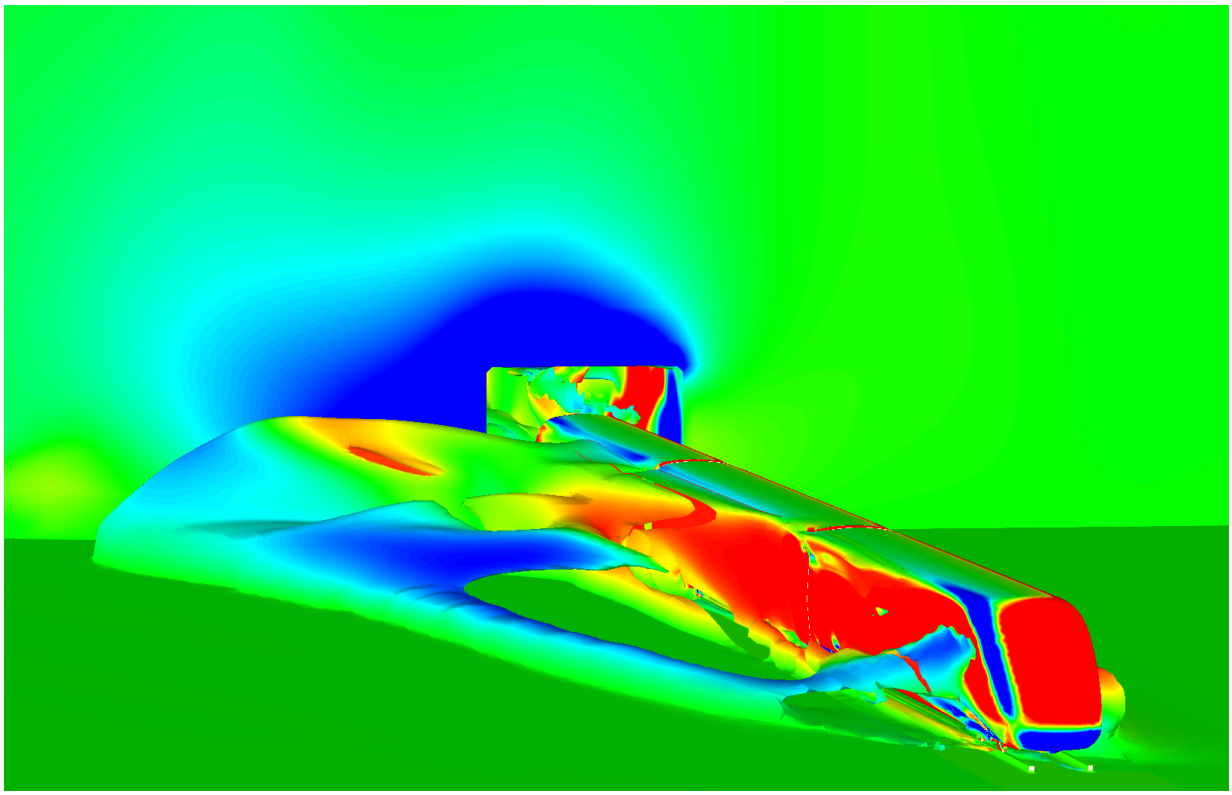

Stability of High Speed Train under Aerodynamic Excitations

Master's Thesis in Solid and Fluid Mechanics

ERIK BJERKLUND
MIKAEL ÖHMAN

Department of Applied Mechanics
Division of Dynamics and Division of Fluid Mechanics
CHALMERS UNIVERSITY OF TECHNOLOGY
Göteborg, Sweden 2009
Master's Thesis 2009:03

MASTER'S THESIS 2009:03

Stability of High Speed Train under Aerodynamic Excitations

Master's Thesis in Solid and Fluid Mechanics

ERIK BJERKLUND
MIKAEL ÖHMAN

Department of Applied Mechanics
Division of Dynamics and Division of Fluid Mechanics
CHALMERS UNIVERSITY OF TECHNOLOGY

Göteborg, Sweden 2009

Stability of High Speed Train under Aerodynamic Excitations
ERIK BJERKLUND
MIKAEL ÖHMAN

Master's Thesis 2009:03
ISSN 1652-8557
Department of Applied Mechanics
Division of Dynamics and Division of Fluid Mechanics
Chalmers University of Technology
SE-412 96 Göteborg
Sweden
Telephone: + 46 (0)31-772 1000

Cover:
Train leaving a tunnel and is hit by a strong side wind.

Chalmers Reproservice
Göteborg, Sweden 2009

Stability of High Speed Train under Aerodynamic Excitations
Master's Thesis in Solid and Fluid Mechanics
ERIK BJERKLUND
MIKAEL ÖHMAN
Department of Applied Mechanics
Division of Dynamics and Division of Fluid Mechanics
Chalmers University of Technology

Abstract

It is important to study the aerodynamic effects on high speed trains, due to both comfort and stability. The Swedish high speed trains are aiming to go at a speed of 250 km/h. The present work closely connects the aerodynamic effects with the vibration dynamics within the train.

Two scenarios are simulated, two trains meeting each other and a train leaving a tunnel and is hit by a strong wind gust (35 m/s). From the aerodynamic part, computational fluid dynamics (CFD) is used with the k-ζ-f turbulence model. To simulate both scenarios a moving mesh needs to be used. From the CFD the moments and forces from the pressure and traction on the train body are calculated, and these loads are taking into a low order mathematical model that simulates the vibration dynamics in the train.

For the scenario with meeting trains the train experiences some slight vibrations, causing discomfort, but has no impact on the stability of the train, but for the scenario with the tunnel and side wind the train has a very high risk of derailment.

From the results of the dynamics simulations a comfort and stability measurements were constructed based on the vibrations in the train car and the risk of wheel climbing. From simulating different speeds of the train it could be seen that the comfort and stability change linearly with the speed. Work was also done to see how much impact the coupling between the car bodies can have on the comfort and stability. A comparison was made to a simple, stiff coupling and one that optimizes a set of passive dampers. It's seen that the coupling can make a difference of around 8% in comfort and stability, which equals an effect of lowering the speed 3-5 m/s.

Semi-active dampers of sky-hook and ground-hook type were also tested in the coupling, but they only showed insignificant changes or changes to the worse.

Keywords: Moving mesh, Wind loads, Coupling, Vibration dynamics, CFD, High speed train, Comfort, Stability

Contents

Preface

In this study the forces from aerodynamic simulations have been used to analyze the vibrational behaviour of a high speed train in respect to comfort and stability. A scenario of two trains meeting and a scenario of a train leaving a tunnel with a strong side wind are simulated. The work has been carried out from September 2008 to April 2009 at the Department of Applied Mechanics, Division of Dynamics and Division of Fluid Mechanics, Chalmers University of Technology, Sweden, with Mikael ï¿½hman as student and Professor Viktor Berbyuk as supervisor for the vibration dynamics and Erik Bjerklund as student and Associate Professor Siniša Krajnović as supervisor for the fluid mechanics.

Aknowledgements

We would like to say our thanks to our supervisors and the department of Applied Mechanics for their support, to Albin Jonsson for his help with the vibration dynamics and to the CFD support at AVL, Dr. Branislav Basara, Andreas Diemath and Jürgen Schneider. A special thanks to AVL for providing the Fire licenses. Without their help this project would not have been possible.

Göteborg April 2009
Erik Bjerklund, Mikael Öhman

1 Introduction

Due to the magnitude of the velocity of a high speed train (HST) the flow around it becomes an increasingly important factor. The unsteadiness and the different forces and moments that start acting on the train have a big impact on the stability of the train and safety and comfort of the passengers. This can probably be countered using damping in the bogies and coupling between the trains. This is the reason behind this project. To find the forces and moments affecting the train and if it's the effects on discomfort and instability can be reduced. In previous studies of HST instabilities it has either been purely aerodynamic or dynamic with simplified aerodynamic forces. In this case it is intended to combine them to get an as accurate simulation as possible.

1.1 Purpose

The purpose of this project is to combine two different fields, aerodynamics and dynamics, to accurately simulate the HST by considering all the forces acting on the train in order to get an accurate model. The goal of this project is to combine the aerodynamic forces that acts on a HST with the dynamics on the trains bogie and coupling. An interesting final result would be to find how sensitive the dynamics in the train is to varying velocity.

From vehicle dynamics side the focus of the project will be two folds:

- Create low-order mathematical and computational models for vibration dynamics and stability analysis of HST taking into account aerodynamic excitations. The models must implement the conventional bogie and conventional car-body coupling functional component mechanical models.

- Using created models simulate the vibration dynamics and study stability of motion of HST for the two scenarios.

1.2 Limitations

Two different scenarios were studied. One where two trains meet each other and one where a single train has left a tunnel and is met by a strong wind gust. The model of the train used for the CFD simulations was an ICE2 train. The train consists of two locomotives and one car in the middle making it symmetrical. It has bogies and inter-car gaps. The parameters for the dynamics model were that of a typical HST. For the meeting trains the simulation was carried out at three different velocities, 67 m/s, 70 m/s and 73 m/s, which correspond to 240, 250 and 260 km/h respectively. For the scenario where the train coming out of a tunnel the speed of the train was 70 m/s and the speed of the wind gust was 35 m/s.

1.3 Approach

The aerodynamics was simulated with AVL-Fire CFD solver. For the double train, two train models were used with a moving mesh to simulate the two trains meeting each other. For the second scenario with the HST coming out of the tunnel a model of a ICE2 train in a simulated windtunnel with a moving crosswind was used. The forces and moments acting on the each train car on one of the trains were then handed over for the dynamics calculations.

The dynamics were simulated with a low order mathematical model using MATLAB and functional components for bogie and coupling. The input were the forces and moments

calculated from the CFD simulations and the forces acting on the wheels from the rail. Unknown parameters, such as damping coefficients in the bogie, were decided by minimizing a cost function for comfort and stability. As a last step, active damping was added to the model.

2 Theory of Aerodynamic Simulations

To solve the flow around the trains CFD was used. CFD is based on the finite volume approach. This means that the conservational principals are applied for the properties describing the behaviour of a matter interacting with its surrounding. The laws of conservation of mass and momentum for a finite volume gives the continuity equation (2.1) and the equation of motion (2.2).

$$\frac{\partial \tilde{\rho}}{\partial t} + \frac{\partial}{\partial x_i}(\tilde{\rho}\tilde{u}_i) = 0 \tag{2.1}$$

$$\tilde{\rho}\left(\frac{\partial \tilde{u}_i}{\partial t} + \tilde{u}_j\frac{\partial \tilde{u}_i}{\partial x_j}\right) = \tilde{\rho}b_i + \frac{\partial \tilde{\sigma}_{ij}}{\partial x_j} \tag{2.2}$$

$$\tilde{\sigma}_{ij} = -\tilde{p}\delta_{ij} + \lambda\delta_{ij}\frac{\partial \tilde{u}_i}{\partial x_i} + \mu\left(\frac{\partial \tilde{u}_i}{\partial x_j} + \frac{\partial \tilde{u}_j}{\partial x_i}\right) \tag{2.3}$$

Combining these together with the constitutive equations and assuming Stokes condition ($\lambda = -\frac{2}{3}\mu$) for an isotropic homogeneous Newtonian fluid (2.3), which air is, one ends up with the instantaneous compressible Navier-Stokes equations (2.4).

$$\tilde{\rho}\left(\frac{\partial \tilde{u}_i}{\partial t} + \tilde{u}_j\frac{\partial \tilde{u}_i}{\partial x_j}\right) = \tilde{\rho}b_i - \frac{\partial \tilde{p}}{\partial x_i} + \frac{\partial}{\partial x_j}\left[\mu\left(\frac{\partial \tilde{u}_i}{\partial x_j} + \frac{1}{3}\frac{\partial \tilde{u}_j}{\partial x_i}\right)\right] \tag{2.4}$$

The Navier-Stokes equations are non-linear partial differential equations and believed to precisely describe any type of flow. However only a few exact solutions exists so the Navier-Stokes equations have to be solved numerically. This is easier done by splitting up the instantaneous variables into a mean and a fluctuating part.

$$\begin{aligned}\bar{\tilde{r}} &= \frac{1}{T}\int_T \tilde{r}(t)dt = R \\ \tilde{r} &= R + r\end{aligned}$$

This is called Reynolds decomposition and the resulting equations are called Reynolds-averaged Navier-Stokes equations (2.5) (RANS). Note that no incompressibility assumption were done in this project.

$$\rho\left(\frac{\partial U_i}{\partial t} + U_j\frac{\partial U_i}{\partial x_j} - \overline{u_i\frac{\partial u_j}{\partial x_j}}\right) = \rho b_i - \frac{\partial P}{\partial x_i} + \frac{\partial}{\partial x_j}\left[\mu\left(\frac{\partial U_i}{\partial x_j} + \frac{1}{3}\frac{\partial U_j}{\partial x_i}\right) - \rho\overline{u_i u_j}\right] \tag{2.5}$$

The decomposition leads to a few extra terms, which lead to more unknowns than equations. This is known as the turbulence closure problem and in order to solve the equations the terms has to be modelled.

Table 2.1: Explanation of variables used in continuum mechanics.

t	Time
p	Pressure
u_i	Velocity vector
x_i	Coordinate vector
b_i	Body force vector
μ	Viscosity
λ	Bulk viscosity
ρ	Density
σ_{ij}	Stress tensor
δ_{ij}	Kronecker delta
r	Arbitrary instantaneous variable

2.1 Turbulence Models

Two important components of turbulent flow is the kinetic energy k and the dissipation ε.

$$k = \frac{1}{2}\overline{u_i u_i} \tag{2.6}$$

$$\varepsilon = \nu \overline{\frac{\partial u_i}{\partial x_j}\frac{\partial u_i}{\partial x_j}} \tag{2.7}$$

The Boussinesq eddy viscosity assumption is that there is an turbulent viscosity that can linearly describe the turbulent flow structures. For the k-ε model the assumption is

$$\nu_t = \frac{\mu_t}{\rho} = C_\mu \frac{k^2}{\varepsilon} \tag{2.8}$$

Using an eddy viscosity model as k-ε the kinetic energy and the dissipation are calculated by solving the modelled transport equations (2.9) numerically.

$$\left.\begin{aligned} \frac{dk}{dt} &= P_k - \varepsilon + B + \frac{1}{\rho}\frac{\partial}{\partial x_j}\left[\left(\mu + \frac{\mu_t}{\sigma_k}\right)\frac{\partial k}{\partial x_j}\right] \\ \frac{d\varepsilon}{dt} &= \left(C_{\varepsilon 1}P_k - C_{\varepsilon 2}\varepsilon + C_{\varepsilon 3}B + \frac{1}{3}k\frac{\partial U_k}{\partial x_k}\right)\frac{\varepsilon}{k} + \frac{1}{\rho}\frac{\partial}{\partial x_j}\left[\left(\mu + \frac{\mu_t}{\sigma_\varepsilon}\right)\frac{\partial \varepsilon}{\partial x_j}\right] \end{aligned}\right\} \tag{2.9}$$

where

$$P_k = \nu_t\left(\frac{\partial U_i}{\partial x_j} - \frac{\partial U_j}{\partial x_i}\right)\left(\frac{\partial U_i}{\partial x_j} - \frac{\partial U_j}{\partial x_i}\right) - \frac{2}{3}\left(\nu_t\frac{\partial U_k}{\partial x_k} + k\right)\frac{\partial U_k}{\partial x_k} \tag{2.10}$$

$$B = -b_i\frac{\mu_t}{\sigma_\rho}\frac{\partial \rho}{\partial x_i} \tag{2.11}$$

The body force term b_i is neglected in this case because of the cold flow. The coefficients used have the following standard values given in table 2.2 [1].

Table 2.2: Coefficients for the k-ε model.

C_μ	$C_{\varepsilon 1}$	$C_{\varepsilon 2}$	$C_{\varepsilon 3}$	σ_k	σ_ε	σ_ρ
0.09	1.44	1.92	0.8	1	1.3	0.9

Another eddy-viscosity model used in this project is the k-ζ-f model [8]. It is an altered version of a $\overline{v^2}$-f model for numerical stability, where special treatment of the wall

normal stress $\overline{v^2}$ is taken. This in order to improve the modeling of the wall effects on the turbulence. The new variable ζ is the velocity scale ratio $\zeta = \dfrac{\overline{v^2}}{k}$. This variable get its own transport equation to be solved. The eddy viscosity in the k-ζ-f model is obtained from

$$\nu_t = C_\mu \zeta k \tau \tag{2.12}$$

and the transport equations are

$$\left.\begin{aligned} \frac{dk}{dt} &= P_k - \varepsilon + \frac{1}{\rho}\frac{\partial}{\partial x_j}\left[\left(\mu + \frac{\mu_t}{\sigma_k}\right)\frac{\partial k}{\partial x_j}\right] \\ \frac{d\varepsilon}{dt} &= \left(C^*_{\varepsilon 1} P_k - C_{\varepsilon 2}\varepsilon\right)\frac{1}{\tau} + \frac{1}{\rho}\frac{\partial}{\partial x_j}\left[\left(\mu + \frac{\mu_t}{\sigma_\varepsilon}\right)\frac{\partial \varepsilon}{\partial x_j}\right] \\ \frac{d\zeta}{dt} &= f - P_k\frac{\zeta}{k} + \frac{1}{\rho}\frac{\partial}{\partial x_j}\left[\left(\mu + \frac{\mu_t}{\sigma_\zeta}\right)\frac{\partial \zeta}{\partial x_j}\right] \end{aligned}\right\} \tag{2.13}$$

The function f is obtained by solving

$$L^2\frac{\partial^2 f}{\partial x_j \partial x_j} - f = \left(C_{f1} + C_{f2}\frac{P_k}{\varepsilon}\right)\left(\zeta - \frac{2}{3}\right)\frac{1}{\tau} \tag{2.14}$$

The turbulent time scale τ and length scale L are given by

$$\tau = \max\left[\min\left[\frac{k}{\varepsilon}, \frac{a}{\sqrt{6}C_\mu |S|\zeta}\right], C_\tau\left(\frac{\nu}{\varepsilon}\right)^{1/2}\right] \tag{2.15}$$

$$L = C_L \max\left[\min\left[\frac{k^{3/2}}{\varepsilon}, \frac{k^{1/2}}{\sqrt{6}C_\mu |S|\zeta}\right], C_\eta\left(\frac{\nu^3}{\varepsilon}\right)^{1/4}\right] \tag{2.16}$$

The coefficient $C^*_{\varepsilon 1}$ are modified in the ε equation by dampening the coefficient close to the wall

$$C^*_{\varepsilon 1} = C_{\varepsilon 1}\left(1 + 0.012/\zeta\right) \tag{2.17}$$

The value of the coefficients shown in table 2.3 are all based on empirical studies [8].

Table 2.3: Coefficients for the k-ζ-f model.

C_μ	$C_{\varepsilon 1}$	$C_{\varepsilon 2}$	C_{f1}	C_{f2}	σ_k	σ_ε	σ_ζ	C_τ	C_L	C_η
0.22	1.4	1.9	0.4	0.65	1	1.3	1.2	6.0	0.36	85

Table 2.4: Explanation of variables used in the turbulence models.

t	Time
p	Pressure
u_i	Velocity vector
x_i	Coordinate vector
b_i	Body force vector
k	Kinetic energy
P_k	Production
ε	Dissipation
μ	Viscosity
μ_t	Turbulent viscosity
ν	Kinematic viscosity
ν_t	Turbulent kinematic viscosity
ρ	Density
ζ	Velocity scale ratio
f	Function implicitly defined by itself
L	Length scale
τ	Time scale
S	Strain rate tensor
σ_*	Model coefficient
C_*	Model coefficient

2.2 Coefficients and Mesh Quality Measurements

The force and moment coefficients are calculated as

$$C_F = \frac{F}{\rho A u^2/2} \tag{2.18}$$

$$C_M = \frac{M}{\rho A L u^2/2} \tag{2.19}$$

where density used for scaling is $\rho = 1.189$ kg/m^3, reference length L=3 m,the reference area A=10 m^2 and u is the speed of the train.

The standard procedure to check the quality of the calculations is to look at the dimensionless wall distance, y^+ and the Courant number, C. The lower y^+ the more resolved the flow is, which means more accurate results. The y^+ is calculated as

$$y^+ = \frac{u_* y}{\nu} \tag{2.20}$$

$$u_* \equiv \sqrt{\frac{\tau_w}{\rho}} \tag{2.21}$$

$$\tau_w = \mu \left(\frac{\partial u}{\partial y} \right)_{y=0} \tag{2.22}$$

where y is the height of the first cell from the wall.

The Courant number of the flow is calculated as

$$C = \frac{u' \Delta t}{h} < 1 \tag{2.23}$$

where u' is the RMS of the velocity and h is the height of cell. The Courant number (CFL number) is supposed to be below one at all times in the entire mesh to ensure that the information travels from one cell to the next. The Courant number can however locally be higher without affecting the flow.

3 Theory of Vibration Dynamics

The equations of motion with springs and dampers give differential equations for $\ddot{x}$ from x and $\dot{x}$. The model could also include PID (proportional-integral-derivative) controller in the active dampers the equations needs to be expanded to take into account the integral of the displacement as well, but in present work such controllers were not considered. We obtain a set of differential equations

$$\ddot{x}_i = f_i[t, \underline{x}, \underline{\dot{x}}] \tag{3.1}$$

In order to solve this numerically it's usefull to rewrite it to a set of first order differential equations. This leads to a set of generalized coordinates expressed as

$$\underline{q} = \begin{pmatrix} \underline{x} \\ \underline{\dot{x}} \end{pmatrix} \tag{3.2}$$

resulting in the form of a set of first order differential equations

$$\underline{\dot{q}} = \underline{\hat{f}}[t, \underline{q}] \tag{3.3}$$

The model is separated into a linear part $\underline{\underline{A}}$ and nonlinear part $\underline{R}$ as

$$\underline{\dot{q}} = \begin{pmatrix} \underline{\dot{x}} \\ \underline{\ddot{x}} \end{pmatrix} = \underline{\underline{A}} \cdot \underline{q} + \begin{pmatrix} \underline{0} \\ \underline{\underline{M}}^{-1} \cdot \underline{R} \end{pmatrix} \tag{3.4}$$

where $\underline{R} = \underline{R}[\underline{q}]$ and

$$\underline{\underline{A}} = \begin{pmatrix} \underline{\underline{0}} & \underline{\underline{I}} \\ \underline{\underline{\widehat{K}}} & \underline{\underline{\widehat{C}}} \end{pmatrix} \tag{3.5}$$

where

$$\underline{\underline{\widehat{K}}} = -\underline{\underline{M}}^{-1} \cdot \underline{\underline{K}} \tag{3.6}$$

$$\underline{\underline{\widehat{C}}} = -\underline{\underline{M}}^{-1} \cdot \underline{\underline{C}} \tag{3.7}$$

The matrices $\underline{\underline{K}}$ and $\underline{\underline{C}}$ depends on which parts that are part of the model. In the case of a single bogie being modeled it's simply

$$\underline{x} = \underline{x}_{b1} \tag{3.8}$$

$$\Longrightarrow$$

$$\underline{\underline{M}} = \underline{\underline{M}}_{b1} \tag{3.9}$$

$$\underline{\underline{K}} = \underline{\underline{K}}_{b1} \tag{3.10}$$

$$\underline{\underline{C}} = \underline{\underline{C}}_{b1} \tag{3.11}$$

and with a single train car with two bogies they are assembled as

$$\underline{x} = \begin{pmatrix} \underline{x}_{c1} \\ \underline{x}_{v1b1} \\ \underline{x}_{v1b2} \end{pmatrix} \tag{3.12}$$

$$\Longrightarrow \tag{3.13}$$

$$\underline{\underline{M}} = \begin{pmatrix} \underline{\underline{M}}_{c1} & \underline{\underline{0}} & \underline{\underline{0}} \\ \underline{\underline{0}} & \underline{\underline{M}}_{c1b1} & \underline{\underline{0}} \\ \underline{\underline{0}} & \underline{\underline{0}} & \underline{\underline{M}}_{c1b2} \end{pmatrix} \tag{3.14}$$

$$\underline{\underline{K}} = \begin{pmatrix} \underline{\underline{K}}_{c1} & \underline{\underline{BK}}_{c1b1} & \underline{\underline{BK}}_{c1b2} \\ \underline{\underline{BK}}^{\mathrm{T}}_{c1b1} & \underline{\underline{K}}_{c1b1} & \underline{\underline{0}} \\ \underline{\underline{BK}}^{\mathrm{T}}_{c1b2} & \underline{\underline{0}} & \underline{\underline{K}}_{c1b2} \end{pmatrix} \tag{3.15}$$

$$\underline{\underline{C}} = \begin{pmatrix} \underline{\underline{C}}_{c1} & \underline{\underline{BC}}_{c1b1} & \underline{\underline{BC}}_{c1b2} \\ \underline{\underline{BC}}^{\mathrm{T}}_{c1b1} & \underline{\underline{C}}_{c1b1} & \underline{\underline{0}} \\ \underline{\underline{BC}}^{\mathrm{T}}_{c1b2} & \underline{\underline{0}} & \underline{\underline{C}}_{c1b2} \end{pmatrix} \tag{3.16}$$

where 1 is for the train car, 2 for the front bogie and 3 for the back bogie and the matrices $\underline{\underline{BK}}$, $\underline{\underline{BC}}$ are the coupling between the car and bogies.

In the simulations where no PID regulator is used, the system is simplified by reducing the first row and first column of $\underline{\underline{A}}$.

The nonlinear forces, $\underline{R}$, can be separated into a set of nonlinear forces

$$\underline{R} = \underline{R}_{contact} + \underline{R}_{wind} \tag{3.17}$$

3.1 Wind Load

The wind load can be expressed as $\underline{R}_{wind}[t]$, or more suitable as $\underline{R}_{wind}[s[t]]$ where $s[t]$ is the location of the train. Expressing the wind loads as a function of the location instead of the time will make it easier to interpolate over different absolute velocities. Interpolating is only suitable if the set of CFD simulations over different train velocities is not to coarse, as the form of the forces and moments, $F[s[t]]$, $M[s[t]]$ should have a similar shape when changing the velocity a little as opposed to $F[t]$ where the trains will pass each other faster. This can be seen in figure 6.12.

When simulating for a higher speed than available from the CFD simulations, extrapolation is done by scaling through the drag, side and lift coefficient.

$$C = \frac{F[u]}{\frac{1}{2}\rho A u^2} = \text{constant} = \frac{F_{u_0}}{\frac{1}{2}\rho A u_0^2} \tag{3.18}$$

$$\Longrightarrow$$

$$F[u] = \frac{1}{2}\rho A u^2 C = F_{u_0}\left(\frac{u}{u_0}\right)^2 \tag{3.19}$$

where u_0 is the closest speed for which forces have been calculated. If the simulated speed is within the simulated domain the forces can be interpolated when expressed as functions of the traveled distance.

3.2 Contact Forces

The contact forces are calculated from creep in the contact plane. The creep is defined as

$$\xi_x = \frac{V_{wheel,x}}{V_0} \tag{3.20}$$

$$\xi_\eta = \frac{V_{wheel,\eta}}{V_0} \tag{3.21}$$

where x is in the longitudinal direction, η is perpendicular x and the normal at the contact point and V_0 is the forward velocity of the train.

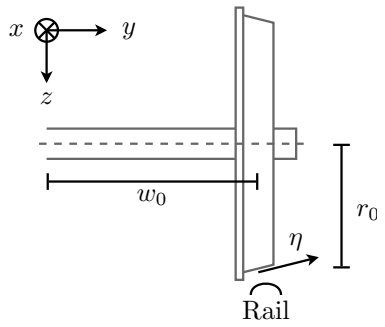

Figure 3.1: Wheelset showing width and radius from center of gravity to nominal contact point.

Right side refers to the right in the forward direction of the train, i.e. the right wheel is shown in figure 3.1.

The velocities can now be calculated as

$$\omega_0 = \frac{V_0}{r_0} \tag{3.22}$$

$$s = \begin{cases} +1 & \text{if right side} \\ -1 & \text{if left side} \end{cases} \tag{3.23}$$

$$r = r[-sx_2] \tag{3.24}$$

$$w = sw_0 - x_2 \tag{3.25}$$

$$\underline{d} = \begin{pmatrix} 0 \\ w \\ r \end{pmatrix} \tag{3.26}$$

$$\underline{\underline{R}}_z = \begin{pmatrix} \cos[-\varphi_3] & -\sin[-\varphi_3] & 0 \\ \sin[-\varphi_3] & \cos[-\varphi_3] & 0 \\ 0 & 0 & 1 \end{pmatrix} \tag{3.27}$$

$$\underline{V}_{wheel} = \underline{\dot{x}} + \begin{pmatrix} V_0 \\ 0 \\ 0 \end{pmatrix} + \underline{\underline{R}}_z \cdot (\underline{d} \times (\underline{\dot{\varphi}} + \begin{pmatrix} 0 \\ \omega_0 \\ 0 \end{pmatrix})) \tag{3.28}$$

where the r is an interpolating function of the geometry of a standardized S1002 wheel profile [7].

Table 3.1: Explanation of variables for calculating the creep.

$\underline{x}$	Translation vector of wheelset.
$\underline{\varphi}$	Rotation vector of wheelset.
r_0	Wheel radius at nominal contact point.
r	Wheel radius at current contact point.
w_0	Lateral distance from COG to nominal contact point.
w	Lateral distance from COG to current contact point.
V_0	Nominal forward velocity of train.
ω_0	Nominal angular velocity of wheels.
δ	Inclination of wheels (positive).
s	Side dependence, +1 for right side, -1 for left side.

3.2.1 Contact Patch Dimensions

To calculate the forces the dimensions of the contact patch are required. According to Hertz theory the dimensions are calculated as [4] and [7]

$$A+B = \frac{1}{2}\left(\frac{1}{r_{\eta,r}}+\frac{1}{r_{\eta,w}}+\frac{1}{r_{x,r}}+\frac{1}{r_{x,w}}\right) \tag{3.29}$$

$$B-A = \frac{1}{2}\left(\left(\frac{1}{r_{x,r}}-\frac{1}{r_{\eta,r}}\right)^2+\left(\frac{1}{r_{x,w}}-\frac{1}{r_{\eta,w}}\right)^2+ 2\left(\frac{1}{r_{x,r}}-\frac{1}{r_{\eta,r}}\right)\left(\frac{1}{r_{x,w}}-\frac{1}{r_{\eta,w}}\right)\cos[2\phi_z]\right)^{\frac{1}{2}} \tag{3.30}$$

$$\Psi = \sqrt[3]{\frac{3N}{2(A+B)}\left(\frac{1-\nu_w^2}{E_w}+\frac{1-\nu_r^2}{E_r}\right)} \tag{3.31}$$

$$\theta = \arccos\left[\frac{B-A}{A+B}\right] \tag{3.32}$$

$$a = m\Psi \tag{3.33}$$

$$b = n\Psi \tag{3.34}$$

where $m = m[\theta]$ and $n = n[\theta]$. There is no explicit expression for $m[\theta]$ or $n[\theta]$ but they can be solved numerically with (4.25) through (4.32) in [11]. This has been done in table 8-1 in [7] which values are used.

Table 3.2: Explanation of variables for calculating the creep.

N	Normal force in contact.
E_w, E_r	Modulus of elasticity in the wheel and rail.
ν_w, ν_r	Poissons ratio for the wheel and rail.
a, b	Contact patch dimension along x and η.
$r_{x,w}, r_{x,r}, r_{\eta,w}, r_{\eta,r}$	Radius around the respective axis for wheel and rail.
ϕ_z	The angle of the wheel.

The radius $r_{\eta,r}$ is zero since the rail is straight. The other radii varies with the contact point and wheel profile. However they are approximated as constant for the contact geometry at a point far from the flange where the wheel is almost flat. In that case $r_{x,w} = \infty$ and $r_{\eta,w} = r$. For the wheel the radius over the top of the rail is almost constant and be approximated as $r_{x,r} = 300$mm. In this case η-axis is parallell with the y-axis. The effect

from the rotation of the wheel is also neglected, as this angle will always be small, i.e. linearisation of $cos[2\phi_z] \approx 1$. This simplifies the equations and with the approximations of the radii the variables m and n are constant.

The rest of the material parameters were set to $E_w = E_r = 200$ GPa and $\nu_w = \nu_r = 0.3$.

3.2.2 Wheel Forces from Creep

The creep forces are calculated with Kalker's linear theory [7]. The coefficients for the creep, $\underline{C} = \underline{C}[\frac{a}{b}]$, are interpolated from a set of data taken from table 8-2 in [7].

$$\underline{F}_{lin} = -Gab \begin{pmatrix} C_{11}\xi_x \\ C_{22}\xi_\eta \end{pmatrix} \tag{3.35}$$

$$u = \frac{|\underline{F}_{lin}|}{\mu N} \tag{3.36}$$

$$\hat{\underline{F}} = \underline{F}_{lin} \begin{cases} 1 - \frac{u}{3} + \frac{u^2}{27} & \text{if } u < 3 \\ \frac{\mu N}{|\underline{F}_{lin}|} & \text{otherwise} \end{cases} \tag{3.37}$$

The behaviour of the flange will be greatly simplified as done in [13]

$$F_{flange} = \begin{cases} k_{flange}(n_{flange} - x_2) & \text{if } x_2 > n_{flange} \wedge s > 0 \text{ (right side)} \\ k_{flange}(-n_{flange} - x_2) & \text{if } x_2 < -n_{flange} \wedge s < 0 \text{ (left side)} \\ 0 & \text{otherwise} \end{cases} \tag{3.38}$$

where F_{flange} acts in the y-axis and is added to F_y.

The force vector $\hat{\underline{F}}$ is here acting on the contact plane, so to get the horizontal component

$$\underline{F} = \begin{pmatrix} F_x \\ F_y \end{pmatrix} = \begin{pmatrix} \hat{F}_1 \\ \hat{F}_2 \frac{\delta}{\sqrt{1+\delta^2}} + F_{flange} \end{pmatrix} \tag{3.39}$$

The contributions to the nonlinear force on the system will be

$$\underline{R}_e = \begin{pmatrix} F_x \\ F_y \\ 0 \\ 0 \\ rF_x \\ -wF_x - wF_y \sin[\phi_3] \end{pmatrix} \tag{3.40}$$

which is assembled into $\underline{R}$ for each wheel.

3.3 Statement of the Vibrational Problem

The problem is divided into two parts, handled separately, stability and comfort. It is necessary to define a single scalar J that is a measurement of how well the system is performing, with $J = 0$ being the perfect case. The goal is to minimize J by changing the dampers in the bogie and introducing active dampers in the coupling.

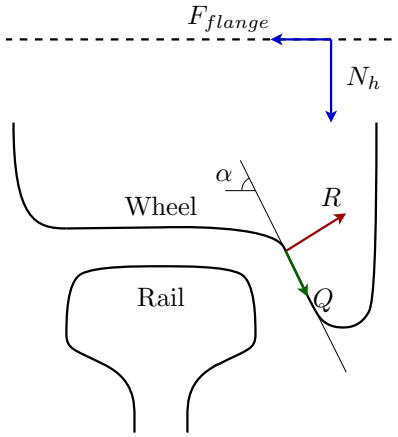

Figure 3.2: Free body diagram for the forces on the wheel when the flange is in contact.

3.3.1 Cost Function for Stability

The flange forces is most critical for safety and may not reach a to high value, since it would mean a high risk of derailment from wheel climb or rail roll. According to [5] a simple measurement of the stability can be constructed by looking at the forces when the flange is in contact. When the wheel starts to climb there will be a single contact point in the flange, shown in figure 3.2. The reaction force R on the flange is solved by summing the forces in the normal direction

$$\nearrow: R - N_h \cos[\alpha] - F_{flange} \sin[\alpha] = 0 \tag{3.41}$$

In this scenario it matters if the wheel is angled towards the rail or not, as the friction orce Q will then change sign. The friction is fully developed and with the coordinate system z vertical downwards the expression for Q is obtained as

$$Q = \begin{cases} \operatorname{sgn}[\phi_3]\mu R & \text{if right side} \\ -\operatorname{sgn}[\phi_3]\mu R & \text{if left side} \end{cases} \tag{3.42}$$

where μ is the friction coefficient between the wheel and rail and α is the flange angle.

Projecting the forces on the flange angle α one obtains the condition for stability as

$$\searrow: N_h \sin[\alpha] - F_{flange} \cos[\alpha] + Q > 0 \tag{3.43}$$

and rearranging the inequality one obtains

$$L = \begin{cases} \dfrac{\tan[\alpha] - \operatorname{sgn}[\phi_3]\mu}{1 + \operatorname{sgn}[\phi_3]\mu \tan[\alpha]} & \text{if right side} \\ \dfrac{\tan[\alpha] + \operatorname{sgn}[\phi_3]\mu}{1 - \operatorname{sgn}[\phi_3]\mu \tan[\alpha]} & \text{if left side} \end{cases} \tag{3.44}$$

$$\frac{|F_{flange}|}{N_h} < L \tag{3.45}$$

where derailment will occur when the inequality is not fullfilled.

This leads to a suitable cost function to minimize

$$F_{s,i} = \left(\frac{F_{flange,i}}{N_{h,i} L_i} \right)^2 \tag{3.46}$$

$$J_{s,1} = \sqrt{\frac{1}{t_1 - t_0} \int_{t_0}^{t_1} \sum F_{s,i} dt} \tag{3.47}$$

where $F_{s,i}$ is calculated for every wheel. The quotient may also not reach a too high value at any time as this would cause derailment.

In addition to $J_{s,1}$, the normal forces on the wheels will also be analyzed, and they should not drop below a certain threshold, calculated as percentage of the static forces, and (3.45) should be fullfilled at all times.

Since the flange might not touch at all if the wind load is to small, i.e. $J_{s,1} \equiv 0$ for all dampers, a secondary measurement is used to analyze the stability. For that, the lateral movement of the wheelsets are analyzed according to

$$J_{s,2} = \sqrt{\frac{1}{t_1 - t_0} \int_{t_0}^{t_1} \sum y_i^2 dt} \tag{3.48}$$

where y_i is the lateral displacement of each wheelset.

3.3.2 Cost Function for Comfort

For comfort the vibration felt by the passenger defines the cost function F. The rotational effect is neglected, leaving only displacement at any given position in the train car.

$$\underline{d}_i = \underline{x}_i + \underline{\varphi}_i \times \overrightarrow{\underline{v}}_i \tag{3.49}$$

$$F_i = |\ddot{\underline{d}}_i|^2 \tag{3.50}$$

$$J_c = \sqrt{\frac{1}{t_1 - t_0} \int_{t_0}^{t_1} \sum F_i dt} \tag{3.51}$$

where $\underline{x}$ is the displacement of a train car and Ω is the domain of the train, i.e. $\overrightarrow{\underline{v}}$ is the vector from the COG to any seat within the train car. This domain is set to seat level, and can be simplified to only the end points of the train, as the displacement must be largest in any of these points.

4 Method for Aerodynamic Simulations

CFD uses finite volumes method which means that a mesh has be created. The cells of the mesh contains the information of the flow. A finer mesh leads to a more accurate result but it also means longer computational time and that more computer resources are needed.

4.1 Mesh Creation

For creating the mesh the CFD tool FameHexa and the CFD software Fire was used. The calculations are done on a ICE2 train geometry. The geometry can be seen in profile in figure 4.1.

Figure 4.1: The geometry of the high speed train ICE2.

The geometry is symmetric and consists of two locomotives and a middle car. It has bogies, wheels and inter-car gaps. The train proportions can be seen in figure 4.2. The width of the train is $W \approx 3$ meters.

The aim of the calculations is to simulate actual trains so the full scale on all the parameters are used. Rails is added to the train geometry for getting the right distance

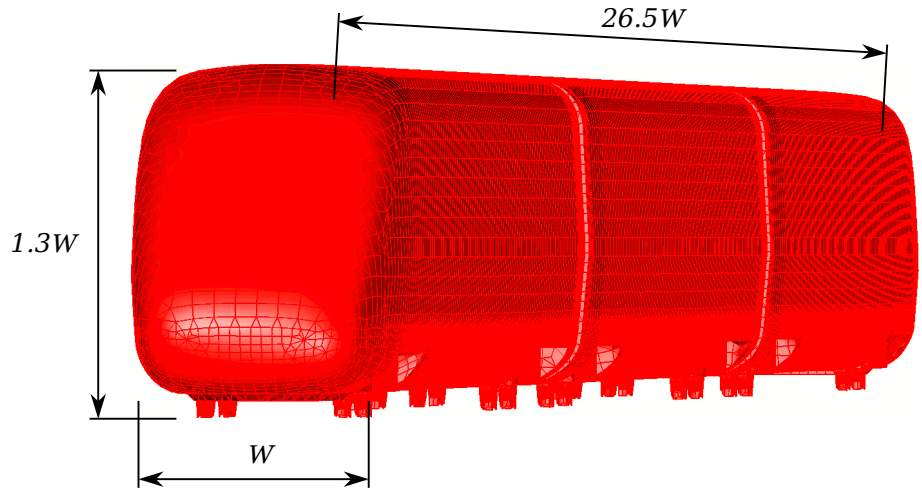

Figure 4.2: The train with its proportions.

from the ground. The height of the rail is 0.18 meters which is standard height of rails in Sweden. However, any effect from sleepers is neglected and is not going to be meshed. In order to be able to mesh the rails they had to be wider then the train wheel which is not the case in reality. A box not much bigger the train itself is created around the train. The reason for adding this box is that inside the box an unstructured automatically generated mix of hexagonal and tetragonal mesh is built. The mesh also have boundary layers on the surfaces of the train ground and rail to better resolve the flow. In figure 4.3 a cut through the mesh is seen.

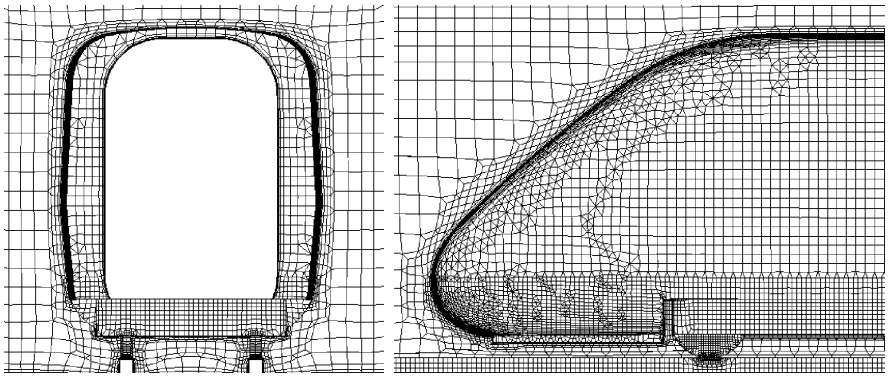

Figure 4.3: Profiles of unstructured mesh.

4.1.1 Mesh Topology for the Two Meeting Trains

The rest of the mesh is then created from the meshed box. The mesh is created from extruding the faces of the box creating a structured grid. The lower part of the domain containing one of the trains can be seen in figure 4.4.

The mesh is then mirrored to obtain the second train. The final topology of the mesh domain can be seen in figure 4.5.

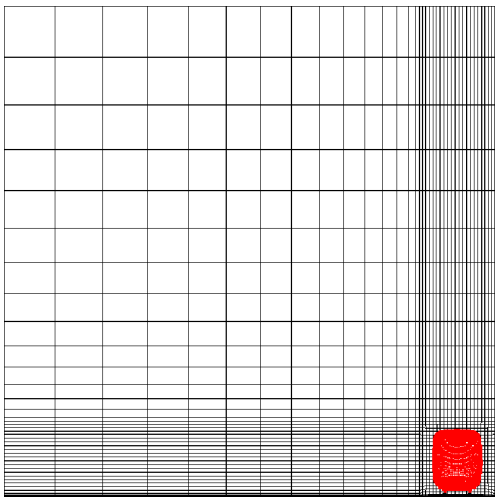

Figure 4.4: The mesh of the lower part of the domain seen from behind.

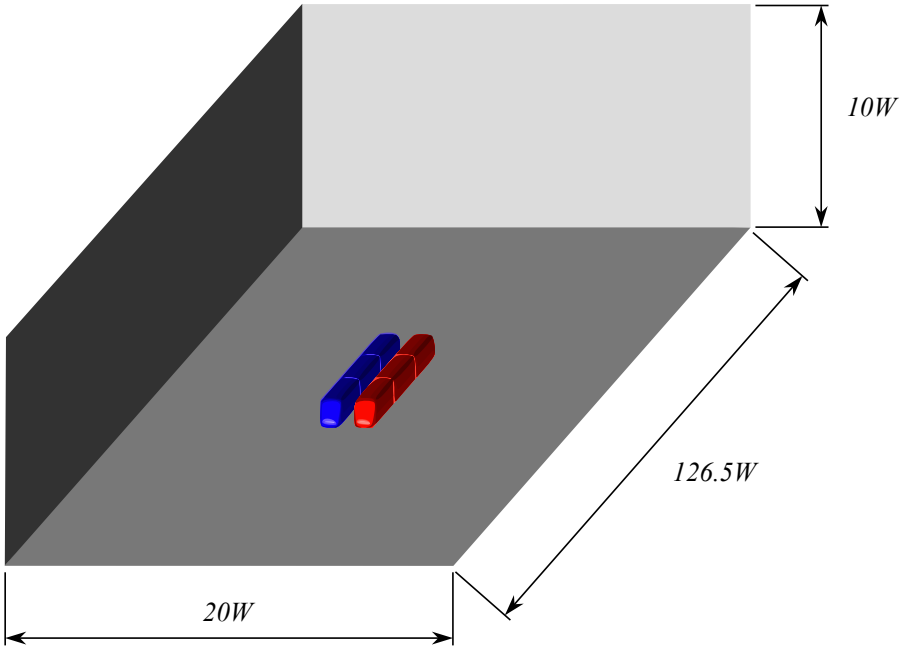

Figure 4.5: The whole mesh domain with both trains.

4.1.2 Mesh Topology for the Train Exiting a Tunnel

The creation of the mesh for the second scenario was done in a similar manner. The box containing the mesh around the train was used to expand the grid creating the tunnel from which the train will exit. The size of the tunnel is the minimum of the standard size used on Swedish tunnels. The shape of the tunnel roof is in reality the shape of half a circle. This could however not be recreated due to the nature of the creation of the mesh. In figure 4.6 the topology for the train coming out of the tunnel can be seen. The wind gust is simulated by setting an inlet for the first $10W$ closest to the tunnel, also seen in figure 4.6. The second tunnel seen in the domain is only used for cell deformation in front of the train. The train itself will never be close to that tunnel.

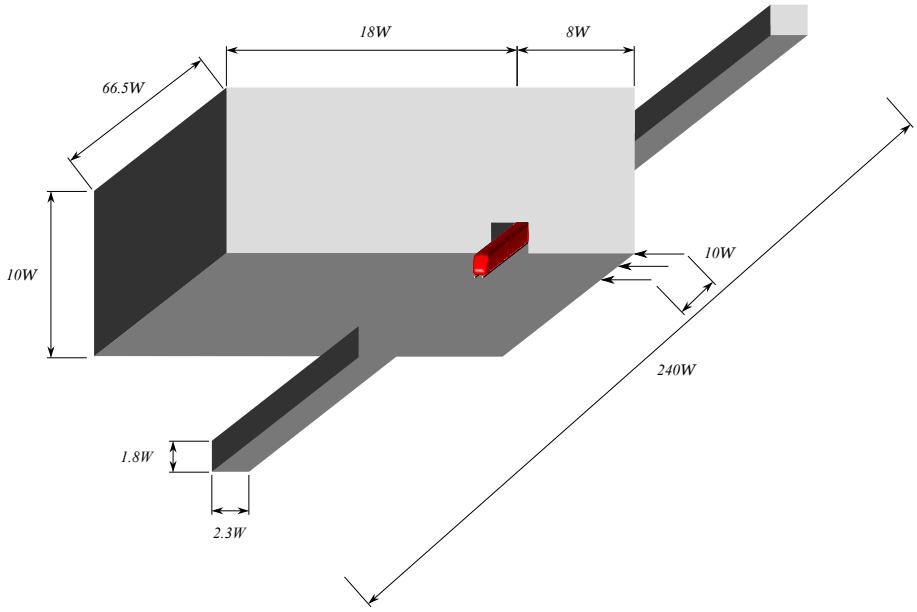

Figure 4.6: The mesh domain for the train coming out of a tunnel.

4.2 Mesh Deformation

A mesh deforming code formula is used and implemented into the CFD calculations in order to get the two trains to meet. The formula makes use of two different objects that it will move in opposite directions on the x-axis. The two objects are two cell selections done on the mesh and they are arbitrary selections. These two selections will remain undeformed and the rest of the mesh can be deformed as much as the movement demands. It is imperative that careful considerations are done before starting the mesh deformation or else the mesh can become skewed or element volumes can become negative which immediately stops the calculations. In figure 4.7 the two selected areas are shown.

In figure 4.7 the trains can be seen meeting. The area around the trains are the selections for the movement. The selected objects for the movement have constant cell sizes and the areas behind and in front the movement are compressed or expanded. The selections are made from wall to wall and from top to bottom of the domain, so only the the cells closest to the in- and outlets are deformed. This fully covering selection makes the mesh only deform in x-direction. The movement is described with a linear function

$$x = \mp L \pm v\ t \tag{4.1}$$

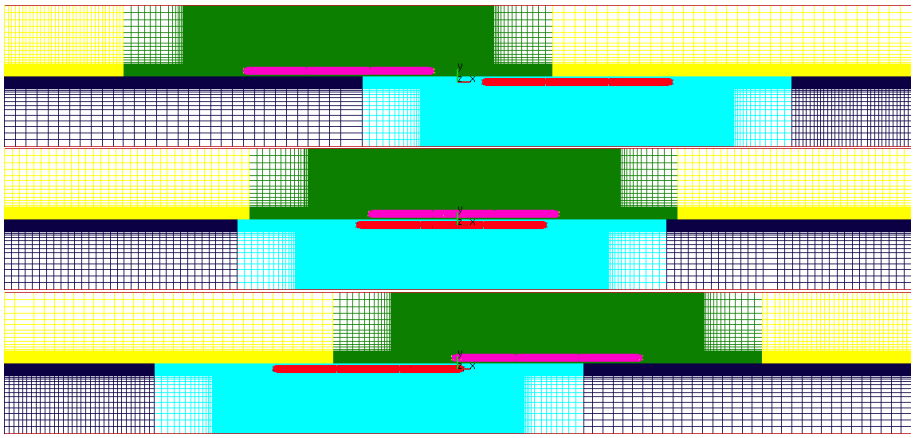

Figure 4.7: The mesh domain with the two trains seen from above at three different timesteps.

where x describes the translation displacement from the origin, the parameter L prescribes the initial displacement from the origin, v is the velocity of the objective and t the current timestep.

The mesh is then mirrored so that the domain is doubled. To connect the two meshes a so called arbitrary interface is used with an arbitrary connetion. This makes the two meshes slide against each other. In figure 4.8 a close up from figure 4.7 shows the sliding interface.

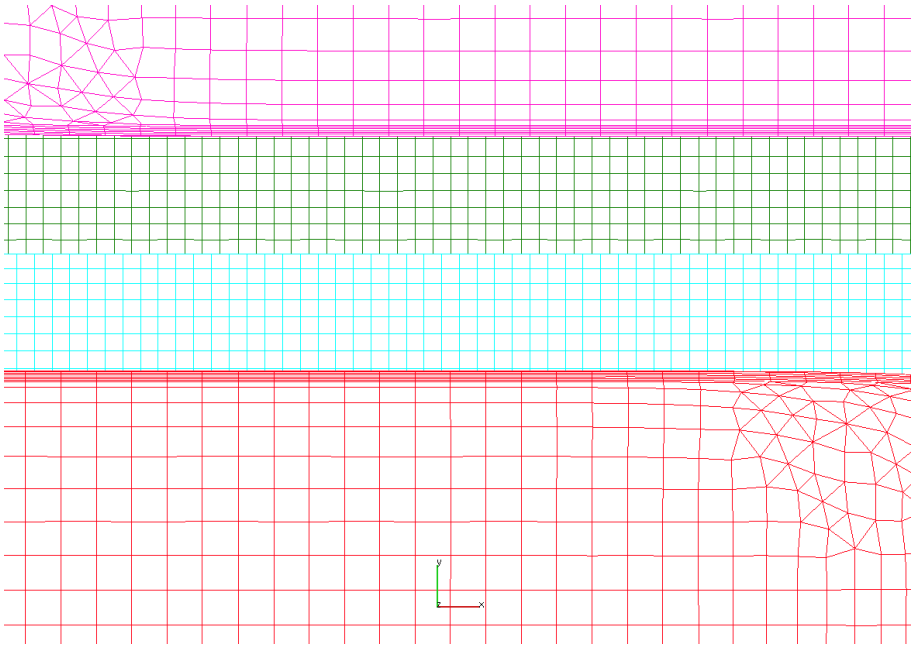

Figure 4.8: The sliding interface seen from above.

To calculate the value of a cell one checks the values of neighbouring cells. However for the cell on the sliding interface the neighbours changes after some timesteps, so the calculation is instead done with coordinates over this arbitrary sliding interface. The cell gives the coordinate of where the neighbouring cell should be and the software checks which cell is on that coordinate and then picks that cell as the neighbour.

For the second scenario with the train coming out of a tunnel only one selection is made for movement, as seen in figure 4.9. A box around the train that slides against three interfaces, the sides and roof of that box, is made. The area closest to the train will be

moving with the train causing these cells to be undeformed. The cells in front and behind will be deformed only in x-direction. The rest of the mesh will be unaffected by the mesh movement.

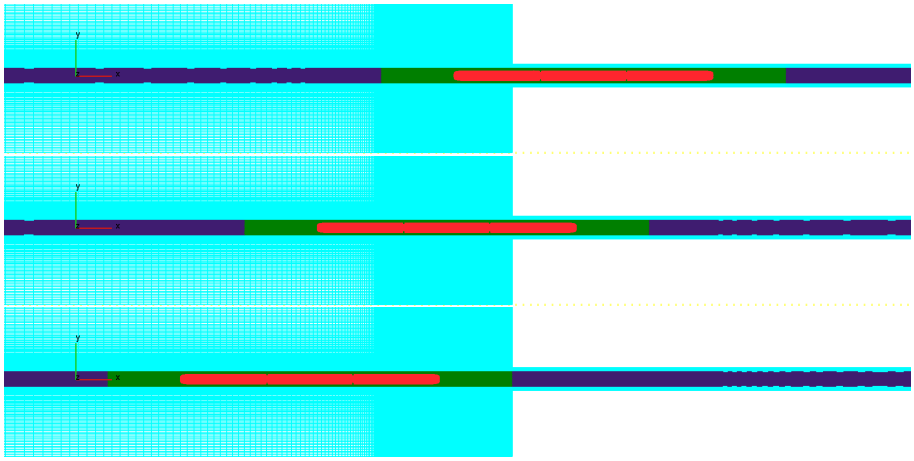

Figure 4.9: The sliding mesh used for the tunnel.

4.3 Setup of CFD Solver

The timestep used were in both cases Δt=0.001 seconds. The two trains were moved 120 meters each and simulated at three different speeds, 67, 70 and 73 m/s. In equation (4.1) L was set to 60 meters. The train coming out of a tunnel was moved 140 meters and simulated at a speed of 70 m/s. For this case L was set to 50 meters in equation (4.1). So from figure 4.5 and 4.6 the trains were moved 60 and 50 meters back or 20 W and 16.7 W respectively. The wind gust hitting it were set to 35 m/s. The boundary conditions were for set to no-slip on the trains and on the walls behind and in front of the trains. Symmetry boundary condition were used at the side walls and on the roof. The ground that moved with the train was set to moving wall at the negative speed of the movement to counter flow phenomenon to appear from the ground, so the selection made for moving the train had a special selection on the floor. The principle was that the no-slip condition on the moving train would create the correct flow.

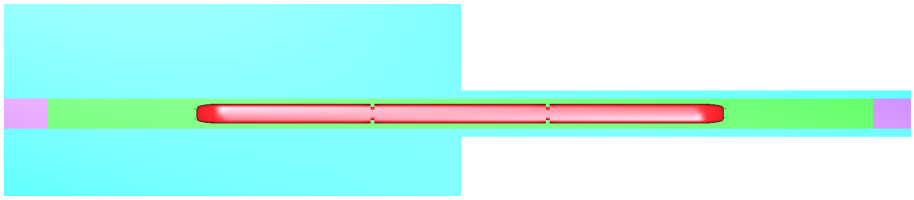

Figure 4.10: The train with the moving ground under it.

The flow is computed as compressible because of the mesh deformation. The k-ζ-f model is the turbulence model that have been used to obtain the final results from the CFD calculations. That is because it is considered a better option than the k-ε model [8]. This project had no intention to compare different turbulence models and there are turbulence models that are more advanced then the k-ζ-f model, but this means that they are more complex to use and more time consuming. Although the results could probably be improved, the k-ζ-f model can be considered sufficient for this project. Hybrid wall treatment,[14] and [3], have been used in both cases. The flow simulated have no change in temperature so the energy equations have not been solved.

5 Method for Vibration Dynamic Simulations

In all dynamic simulations the coordinate system will have the x-axis in the longitude direction, and the z-axis vertically downwards which is the same as the standard in flight dynamics. This means that the force and moments from the CFD simulations will have to change signs for longitude, vertical, roll and yaw.

Table 5.1: Data for the train car.

m	I_x	I_y	I_z
35000[kg]	90×10^3[kgm^2]	1.8×10^6[kgm^2]	1.8×10^6[kgm^2]

The train will be expressed in a system of rigid bodies connected with linear springs and dampers, and for some simulations also a set of nonlinear connectors in the coupling between the cars. The actual train car is modeled as a single rigid body, connected to a bogie frame. Its mass and mass moment of inertia is in table 5. The center of mass was estimated to be at 1.22 meters from the top of the rail. The bogies are connected at ± 9 meters from the center of the car.

5.1 Bogie model

Figure 5.1: Reference photo of the bogie used in high speed trains.

The most important part of the system are the bogies. The bogie used in figure 5.1 has been tested in speeds up towards 300 km/h within the Gröna Tåget research programme. Two mechanical models have been developed and both describe the same bogie. The first model is more complicated, and is made to as accurately as possible describe the behaviour of the real bogie, and a second conventional bogie model for easier comparison with other work on train dynamics.

5.1.1 Degrees of Freedom

To simplify the contact behaviour the vertical displacement and the roll of the wheelsets are locked in the simulations. The small vertical movement and roll which would occur when the wheelset moves laterally is very small, and can be assumed to be zero with little effect on the train dynamics. This also means that the wheelset will hold the train in place, i.e. the normal contact force can be negative, but at that point the instability of the train will be over any acceptable criteria.

The axle boxes are also neglected. The pitch on the wheelsets can rotate freely with respect to the bogie, and the pitch of the axle box is not included in the degrees of freedom. For the displacement and yaw degrees of freedom the wheelset and axle box are merged.

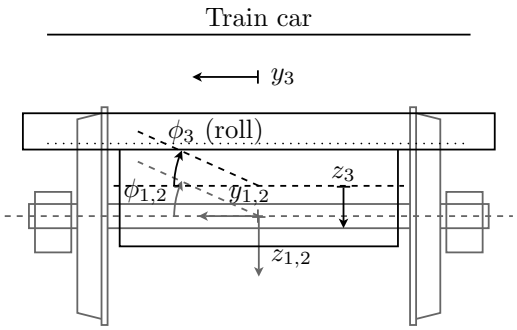

Figure 5.2: Front of bogie showing degrees of freedom.

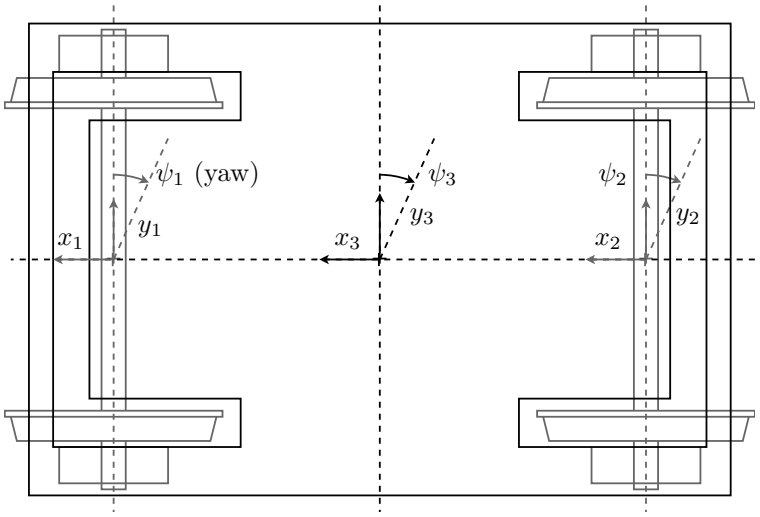

Figure 5.3: Top of bogie showing degrees of freedom.

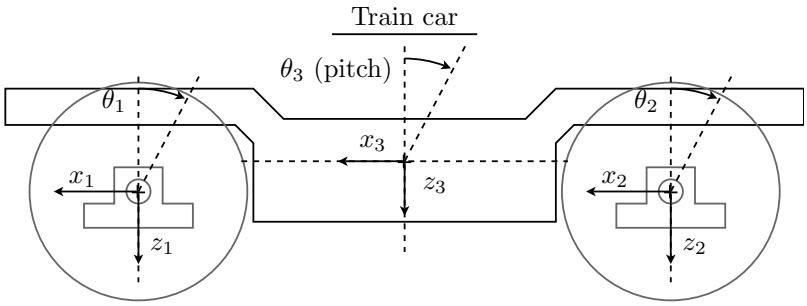

Figure 5.4: Side of bogie showing degrees of freedom.

5.1.2 Geometry of Bogie

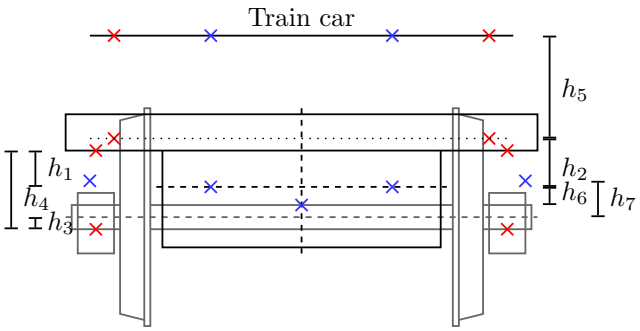

Figure 5.5: Front of bogie showing geometry.

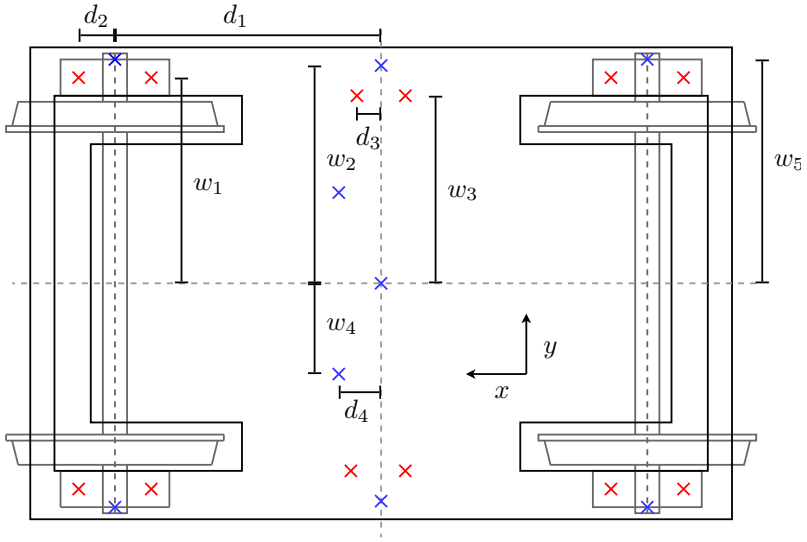

Figure 5.6: Top of bogie showing geometry.

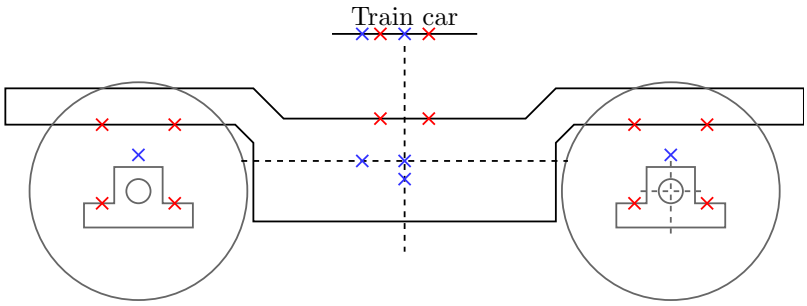

Figure 5.7: Side of bogie showing geomtry.

The bogie is simplified to two symmetry planes shown in figure 5.6.

5.1.3 Placement of Springs and Dampers

All springs and dampers are modeled with momentless joints, so a pair of horizontal springs have been added to each real vertical spring to simulate the horizontal stiffness and rotational stiffness of the bogie. The horizontal springs and dampers will be modeled with

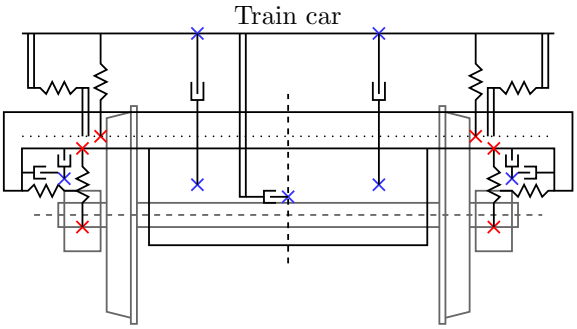

Figure 5.8: Front of bogie showing springs and dampers.

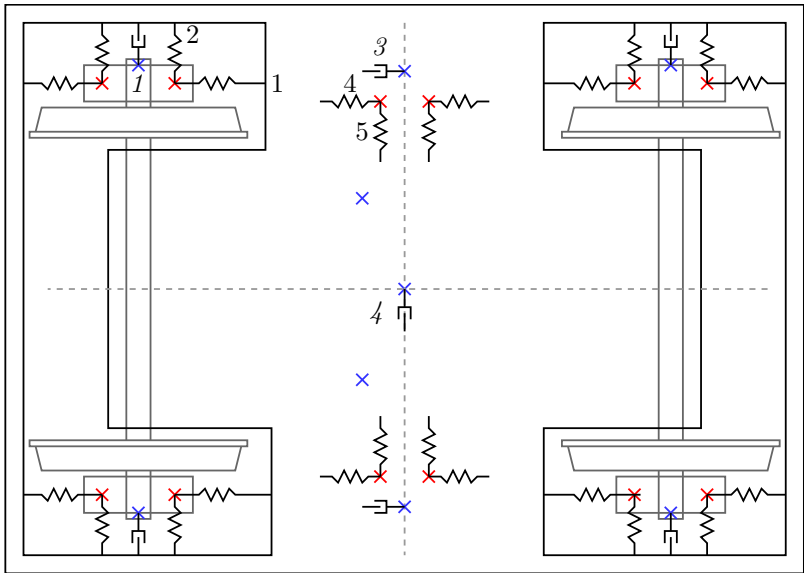

Figure 5.9: Top of bogie showing springs and dampers.

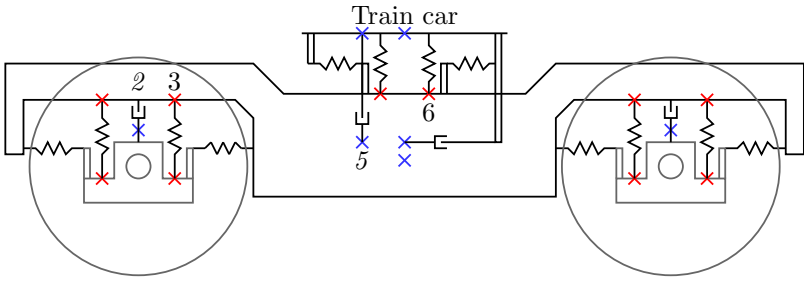

Figure 5.10: Side of bogie showing springs and dampers.

zero relaxed length and is connected to the same point as the vertical spring at both ends, marked by red crosses for springs and blue crosses for dampers in figure 5.5 to figure 5.10. The model also assumes symmetry along both the x-axis and y-axis shown in figure 5.6.

The two vertical springs connecting the bogie to the train were changed to four vertical springs (9 to 12 in figure 5.6) placed at the distance d_3 in order to carry the moment between the bogie and train car. The spring stiffness and the distance d_3 are to be adjusted according to the real springs vertical strength and bending strength.

Table 5.2: Spring and damper coefficients for the bogie. Numbers are shown in figure 5.9 and 5.10.

	Spring[kN/m]	Damper[kNs/m]
1	2500	$100/\sqrt{2}$
2	400	$100/\sqrt{2}$
3	500	900
4	90	15
5	90	15
6	90	-

Table 5.3: Geometry of the bogie. Numbers are shown in figure 5.6, 5.7 and 5.5.

	d[m]	w[m]	h[m]
1	1.3	0.9	0.2
2	0.1	1.1	0.25
3	0.1	0.9	-0.04
4	0.2	0.5	0.2
5	-	1.2	0.2
6	-	-	0
7	-	-	0.04
8	-	-	0

The second bogie model implemented as a conventional bogie [10] with an additional spring between bogie and train car was added.

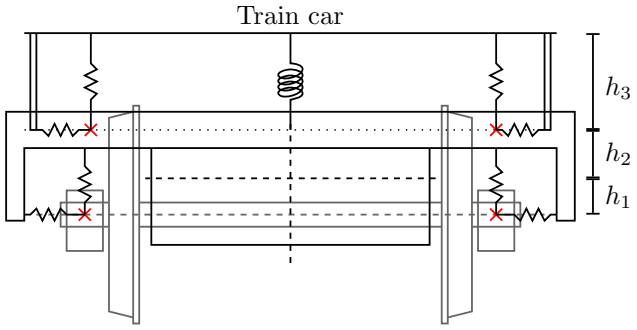

Figure 5.11: Front of conventional bogie showing springs.

For the conventional bogie model the placement is in figure 5.11, 5.12 and 5.13. Every spring is in parallell with a damper which is not shown in the figures.

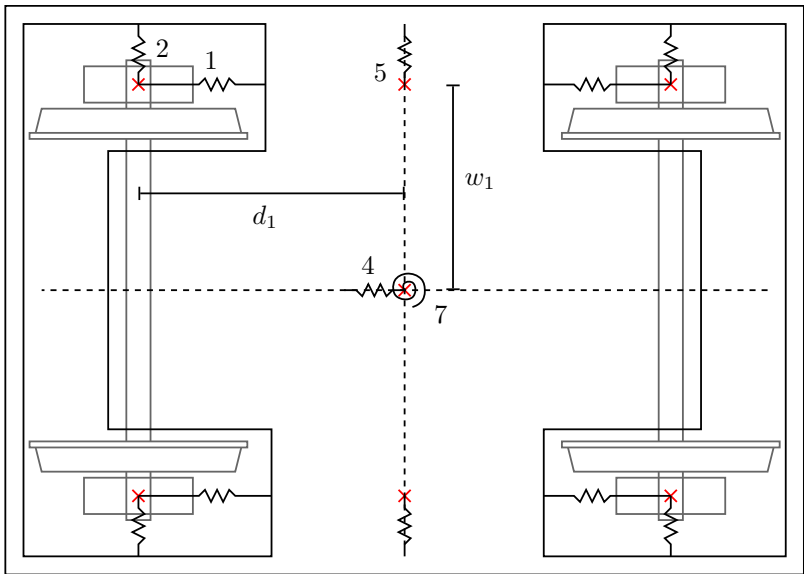

Figure 5.12: Top of conventional bogie showing springs.

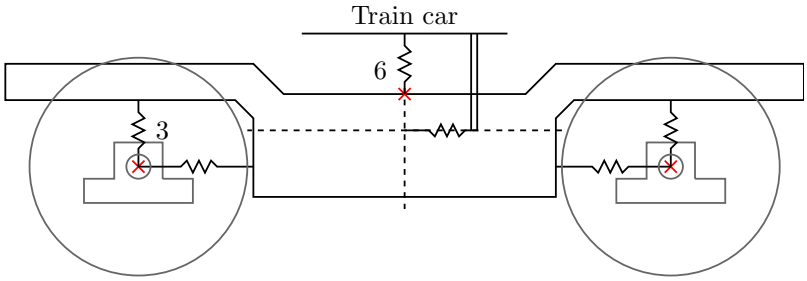

Figure 5.13: Side of conventional bogie showing springs.

Table 5.4: Initial spring and damper coefficients for the conventional bogie. Numbers are shown in figure 5.12 and 5.13.

	Spring	Damper
1	5000[kN/m]	0[kNs/m]
2	800[kN/m]	$100/\sqrt{(2)}$[kNs/m]
3	1000[kN/m]	$100/\sqrt{(2)}$[kNs/m]
4	360[kN/m]	1800[kNs/m]
5	180[kN/m]	7.5[kNs/m]
6	180[kN/m]	4.629[kNs/m]
7	292[kNm]	2178[kNsm]

Table 5.5: The mass and area moment of inertia for both types of bogies.

Part	Mass [kg]	I_x [kgm^2]	I_y [kgm^2]	I_z [kgm^2]
Wheelset	1109	605.9	61.6	605.9
Frame	1982	2670.0	1400.0	2670.0

Using the data in table 5.1.3 the simulations show a very similar behaviour to the more complex bogie model. It is however not possible to fullfill the correct model with the conventional bogie model. Comparing the stiffness matrices the diagonal elements are very close in both models, except for vertical and roll damping in the secondary suspension. The value of of c_6 was adjusted to fullfill the roll damping, as it was believed to have higher impact on the simulations.

5.2 Optimization of the Coupling

Table 5.6: Initial guess of the spring and damper coefficients for the passive coupling.

	Spring	Damper
Longitude	150[MN/m]	300[kNs/m]
Lateral	20[MN/m]	100[kNs/m]
Vertical	30[MN/m]	110[kNs/m]
Roll	300[kNm]	5[kNsm]
Pitch	300[kNm]	5[kNsm]
Yaw	100[kNm]	0.5[kNsm]

One of the main purposes of this work is to see what can be achieved in the coupling between two trains. The coupling is greatly simplified as a single point between the cars where only the relative motion between the cars is meassured. The coupling point is located at the same height at the center of mass of the train car, and at 13 meters from the center in longitude. As a first step, a set of passive springs and dampers are used, for which the damping coefficients were optimized with respect to J_s and J_c separately. The initial guess is written down in table 5.6. The spring constants are very high and simulate a near stiff coupling between the cars.

An additional coupling model is also simulated that allows for larger lateral movements between the cars. To simulate this the spring stiffness in the lateral axis is dropped significantly and the three parameters $k_{lateral}$, $c_{lateral}$ and c_{roll} are going to be optimized. Vertical and longitudinal movement, as well as pitch and yaw, between the cars cannot be high enough without derailment, and it will be hard to efficiently use dampers on these.

For the resulting optimized parameters a sky-hook damper is tested in the coupling. It's maximum value is set to the passive dampers, and the minimum value to a fraction of these.

5.3 Computational Model

The computational model is very close to the mathematical model as a solver for ordinary differential equations (ODE) will be used. When enabling the wheel-rail contact the set of working solvers was greatly reduced as most of them failed to take sufficient time steps. This is typically a trait that loosely defines a stiff ODE system, i.e. an ODE system is stiff if its numerical solution by some solvers requires a significant depression of the step-size to avoid instability [9].

5.3.1 Choice of the ODE Solver

Table 5.7: Available ODE solvers in MATLAB.

	Problem type	Order of accuracy	Time
ode45	Nonstiff	Medium	∞
ode23	Nonstiff	Low	∞
ode113	Nonstiff	Low to high	∞
ode15s	Stiff	Low to medium	Fast
ode23s	Stiff	Low	Fast
ode23t	Moderately Stiff	Low	Untested
ode23tb	Stiff	Low	Untested

With the information from the MATLAB help manual [2] the first solver to try should be ode45. If it woudl fail because the problem is to stiff go on and instead try ode15s. The slightly higher accuracy of ode15s compared to other ODE solvers makes it a suitable choice for all simulations. It would be possible to estimate the stiffness factor of the system, taking the determinant of the Jacobian, but it was not considered necessary.

5.3.2 Automatic Construction of the Stiffness Matrices

Even for a low order mathematical model, assembling the stiffness matrix for the linear contribution manually is time consuming and error-prone. For a complete train with one passenger car and two locomotives this results in a minimum of 21 parts and 102 degrees of freedome.

An algorithm similar to that of assembling a stiffness matrix was implemented to automatically assemble the stiffness and damping matrices. The following algorithm doesn't support rotational springs as only one such spring is in use and it was added manually.

```
% function [X] = StiffnessConstructor(pxtot,xconp,vx)
% Helper function for models. Used for constructing K or C.
% Input:
%   x     :   [3xnx2] Coordinates from cog on each connected part
%   c     :   [2xn]   Coupling matrix (to which part)
%   v     :   [3xn]   List of "springs" with directed stiffness [x,y,z]
%                     n = Number of "springs", any integer >= 0
% Output:
%   X   : [6*nx6*n] "Stiffness" matrix

function [X] = StiffnessConstructor(p,c,v)
    parts = max(c(:));
    X = zeros(parts*6);
    for i = 1:size(v,2)
        L1 = p(:,i,1); % Vector from COG to spring connection
        L2 = p(:,i,2); % and the same for the other end of the spring
        Xe = zeros(12);
        for j = 1:12
            dof = zeros(12,1); dof(j) = 1; % change in dof (unit size)
            t1 = dof(1:3); t2 = dof(7:9); % Split up the dof-vector
            r1 = dof(4:6); r2 = dof(10:12); % and into rotation
            d = t2 + cross(r2,L2) - (t1 + cross(r1,L1));
            f1 = v(:,i).*d; % Multiply displacement with directional stiffness
            f2 = -f1;
            m1 = crossf(L1,f1); % And the moments
            m2 = crossf(L2,f2);
            Xe(:,j) = [-f1;-m1;-f2;-m2]; %
        end
        edof1 = (1:6)+(c(1,i)-1)*6; % The degrees of freedom that these loads
        edof2 = (1:6)+(c(2,i)-1)*6; % corresponds to.
        edof  = [edof1,edof2]; % Element degree of freedom vector
        X(edof,edof) = X(edof,edof) + Xe; % Assembles the full stiffness matrix
    end
end
```

The algorithm is suitable for any multibody system with springs or dampers and was mainly used to calculate the stiffness contribution from the bogies.

6 Results from Aerodynamic Simulations

The primary objective of the results from the aerodynamic simulations is to be used in the dynamic calculations. The results from the scenarios differs greatly from each other. It is interesting to study where the different forces come from and why they behave like they do.

6.1 Two Trains Meeting at High Speed

In figure 6.1 one can see the upcoming impact from the two trains passing each other at high speed. The distribution of the pressure can be seen on the train bodies as well as vortices created from the tail of the train.

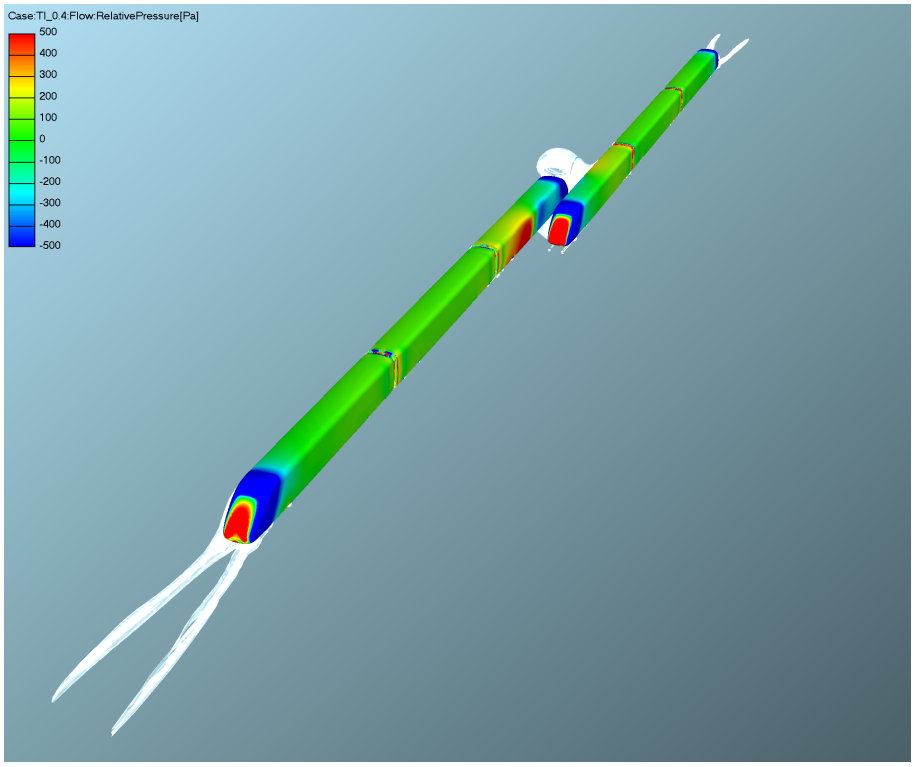

Figure 6.1: The meeting of two trains.

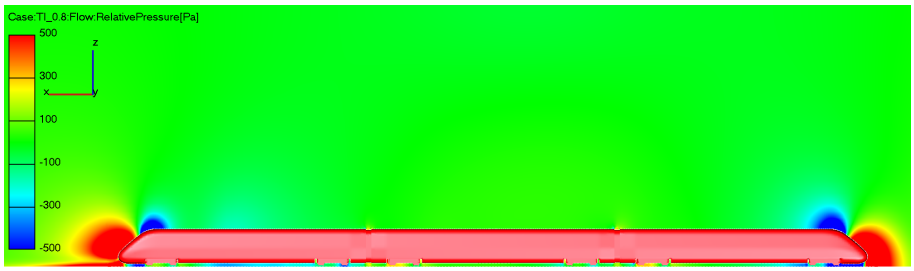

Figure 6.2: The relative pressure acting on the train.

The relative pressure on the train is seen in figure 6.2. This profile is taken from the left train in figure 6.1. This is the characteristic profile of where the pressure is high and

low, but the spectrum on the colorbar is reduced in order to see the more subtle variations. This means that the maximum and minimum values cannot be obtained from the figure.

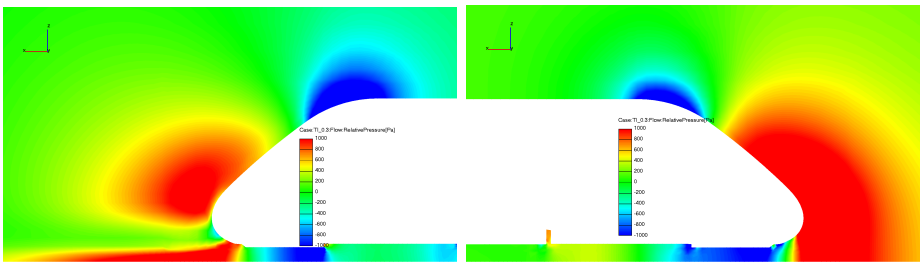

Figure 6.3: Relative pressure on tail and nose.

In figure 6.3 a zoomed view on the tail and the nose of the train can be seen. The train is traveling from left to right so the tail is on the left side and the nose on the right side. There is a large section of low pressure in close vicinity to the high pressures. The big pressure differences will affect the meeting train.

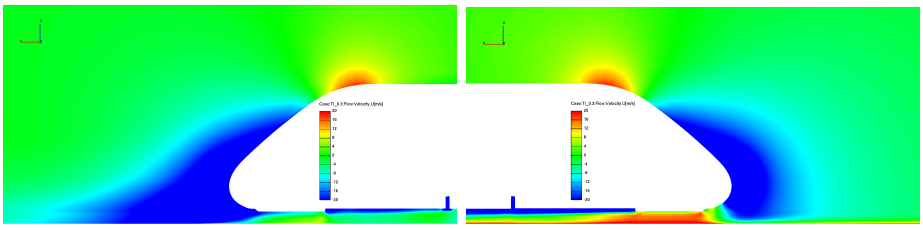

Figure 6.4: Velocity in x-direction around tail and nose.

To see some correlation between the pressure and the velocity one can study the velocity U in x-direction in figure 6.4. A high velocity means a low pressure on the train. The biggest difference is seen on the tail where the vortices are. The vortices are however created the other two velocities V and W in the y and z-direction.

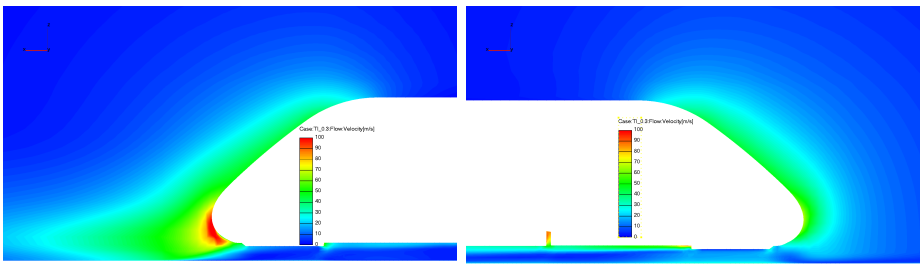

Figure 6.5: Velocity magnitude around tail and nose.

One can also study the magnitude of the velocity on the tail and nose. This is seen in figure 6.5. The highest velocity is on the very front and very back of the train.

The velocity vectors show the direction of the velocity in figure 6.5 in figure 6.6. The vectors are not scaled to its speed and the direction is projected onto this cut.

How this affects the other train for different positions can be seen in figure 6.7. The left picture is the noses of the trains from timestep 0.4 s or position 28 m. The right is the tails of the trains from timestep 1.2 s or position 84 m. The high and low pressure from

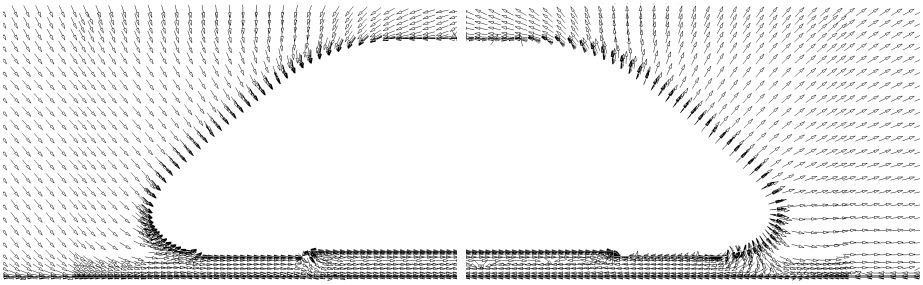

Figure 6.6: Velocity vectors around tail and nose.

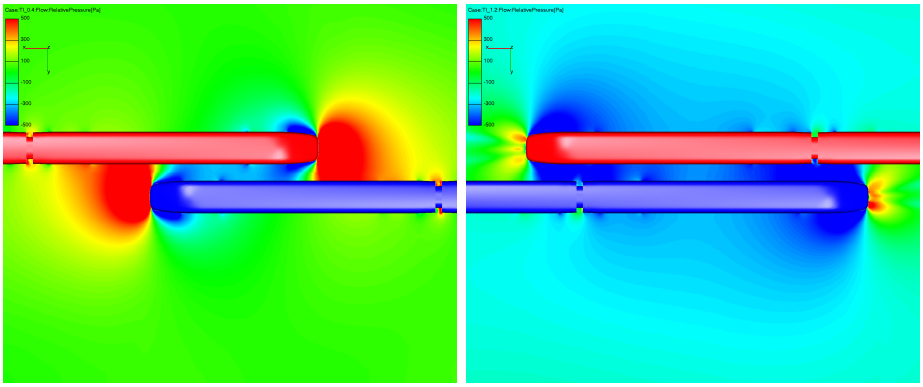

Figure 6.7: High and low pressure on the train at different positions seen from above. The upper train is moving from left to right.

the nose of the trains is having a great influence on the meeting train. Same thing goes for the low and high pressure from the tail of the trains.

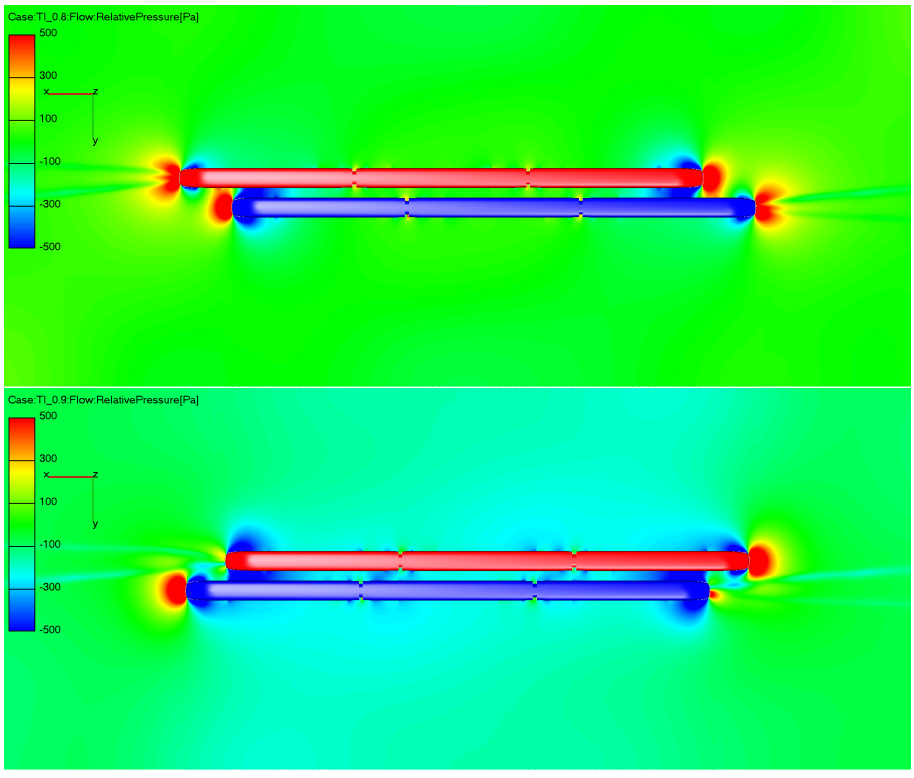

Figure 6.8: The relative pressure around the train.

The alignment of the trains are what gives one of the most interesting effects. The high

pressure on the nose and the tail is aligned at the same time as the low pressures are. This gives an overall low pressure that affects almost the whole train at the same time. The time steps before and after the alignment can be seen in figure 6.8 which is time step 0.8 s and 0.9 s corresponding to 56 m and 63 m respectively.

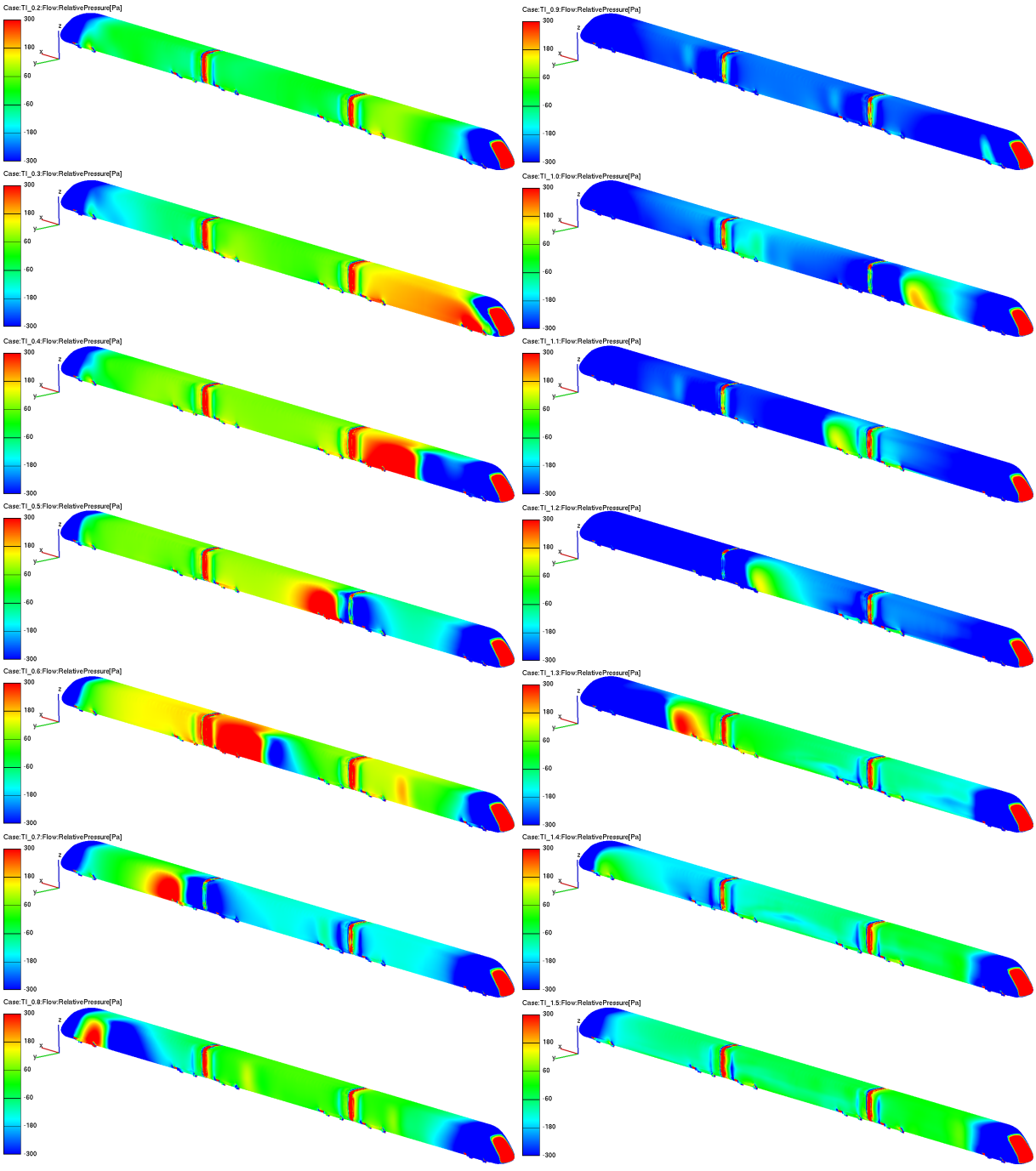

Figure 6.9: The relative pressure acting on the train.

The pressure on the body of the train will determine the forces and moments. In figure 6.9 the relative pressure from time 0.2 seconds to 1.5 seconds which corresponds to position 14 to 105 meters is shown. The first and the last timestep the train is almost unaffected by the meeting train. The distribution of pressure can be seen changing from timestep to timestep. The first timesteps show how the influence from the nose of the oncoming train is going from one end to the other. The pressure then shifts to be over all lower and the influence of the tail from the oncoming train can be seen instead.

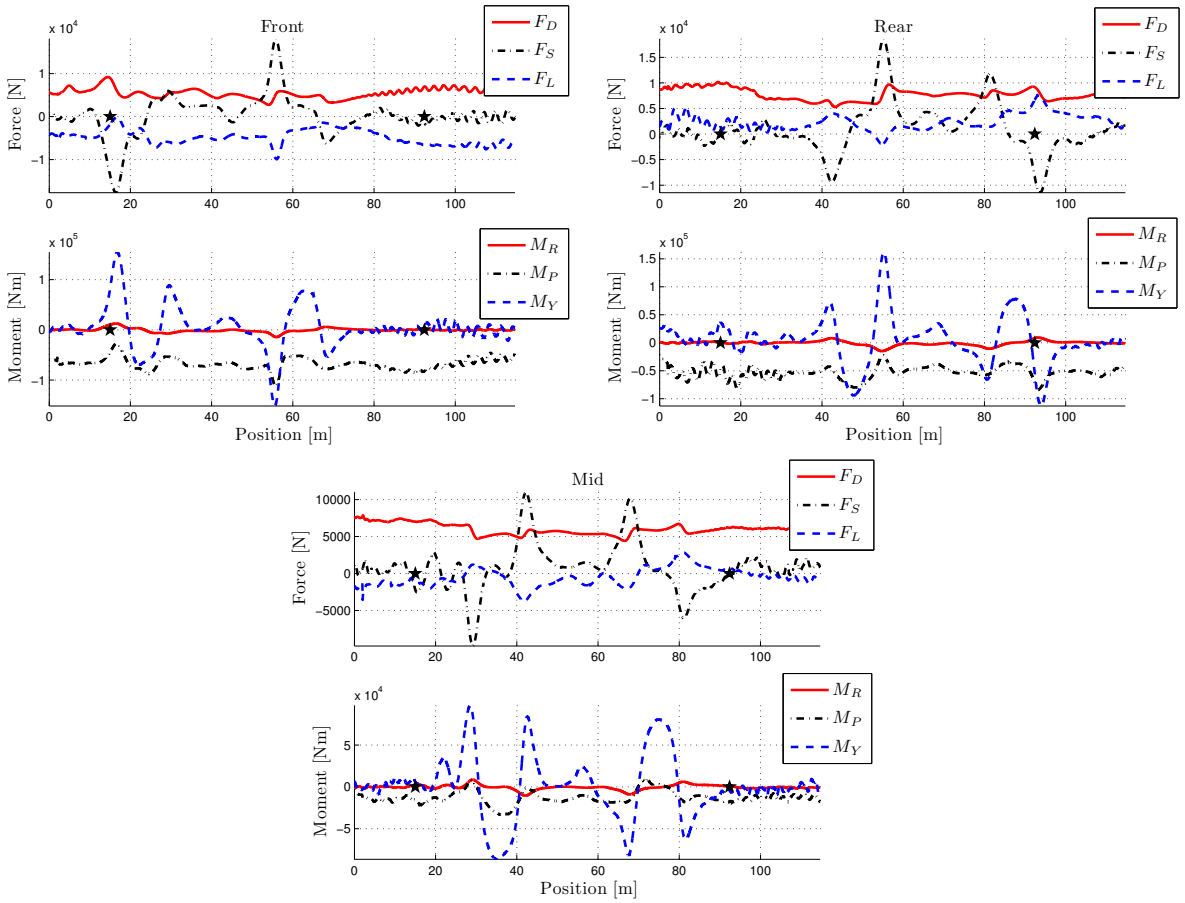

Figure 6.10: The forces and moments acting on the train cars.

For the purpose of calculating the forces and moments the train is split up into three parts, one for each car. These three cars will be called front, middle and rear car. The forces are integrated in each direction from the relative pressure and shear forces. The shear forces are small and do not affect the total force much. The moments are also taken from integration on each car. The train that the results are taken from is the upper one in for example figure 6.8 which is the left one in figure 6.1. The results are not entirely the same for both trains, but the differences are negligible so there is no reason in covering both trains. The train which the results are taken from is going in negative x-direction and the meeting train is in positive y-direction and the z-direction is positive going upwards. This leads to that a high positive drag force, a negative side force means that the train is pushed away from the other train and a negative lift force is down force on the train.

The forces and moments acting on the three different cars can be seen in 6.10. The stars in the graphs mark where the front nose of the trains are aligned when they meet and where the back tails are aligned when they leave each other. The trains moved 120 meters each at constant speed, 70 m/s. The position of the train on the x-axis of the figures is described by (4.1). The biggest force is the side force and the biggest moments is the yaw moment. For the dynamics the mean of F_D, F_L and M_P are removed as the vibration dynamics only simulates the fluctuations, i.e. these will be non-zero for a single train traveling forward.

The side force have four distinct peaks seen in figure 6.11. The first peak is negative which means that the train car is pushed away from the meeting train. The second and third peak implies that the car is pulled towards the meeting train and the fourth peak means that the train car is pushed away from the meeting train again.

The pattern of the four force peaks repeats itself. This results in great changes of the

yaw moment. Note that the first two side force peaks result in negative yaw moment peaks and the last two side force peaks result in positive yaw moment peaks. The transition of two force changing sign give the moment of opposite signs of the peaks. The roll moment of the cars are very much dependent on the position of the center of gravity of the cars. This is not known so an estimation is made.

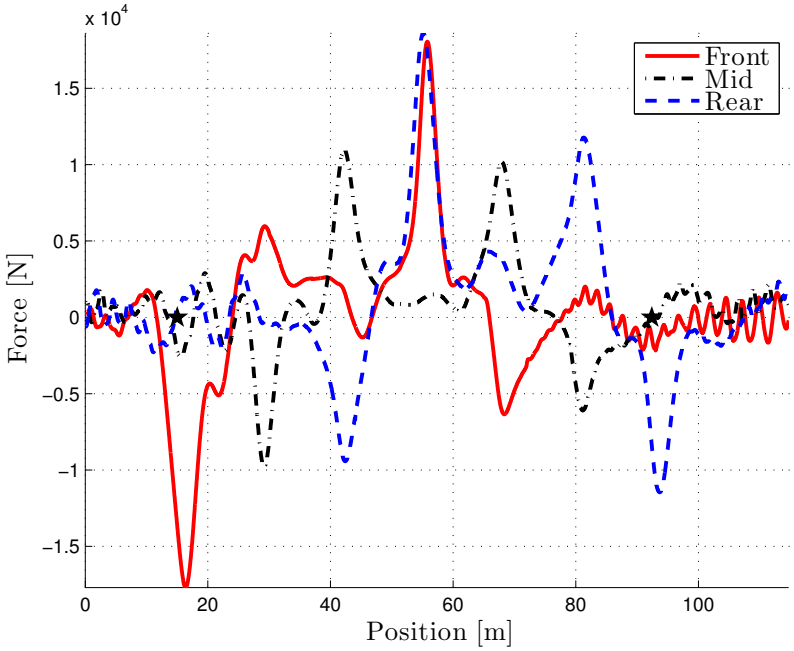

Figure 6.11: Side force on the different cars meeting another train at 140 m/s.

The side force on the different cars can be seen in figure 6.11. One can observe how the forces from the meeting of the other train is going from one car to the next. The force travels with double the speed of one train, i.e their relative speed, 140 m/s.

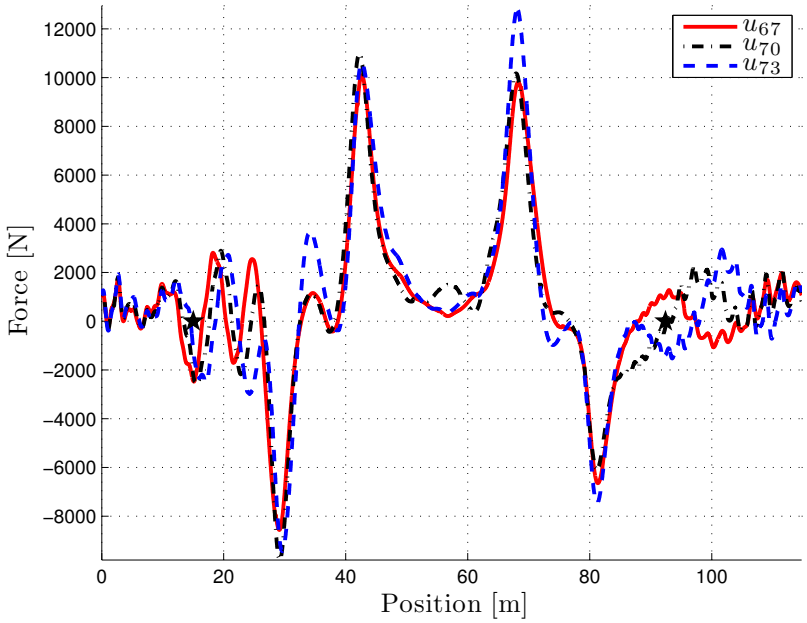

Figure 6.12: Side force on the middle car at speed 67, 70 and 73 m/s.

The forces on the middle car at three different velocities can be seen in figure 6.12. There is not much difference between them in magnitude. In general the higher the velocity the bigger the force. However for the the first two peaks the highest amplitude is from the 70 m/s case. And the last peak the 67 m/s case is higher then the 70 m/s one. The differences between the speeds are not big, but at these small changes the forces already differ a bit in behaviour.

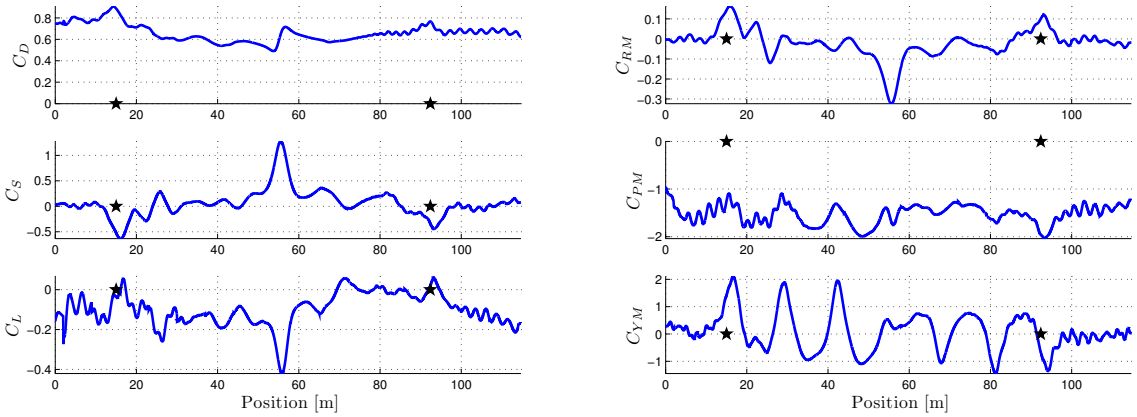

Figure 6.13: The force coefficients on the train from meeting a train at 140 m/s.

The forces and moments on the whole train traveling at 70 m/s can also be studied and seen in figure 6.13. The force coefficients are on the left and the moment coefficients are on the right. There is a distinct force amplitude when the trains are aligned with each other. This is when the forces from low pressures from the front car and rear car collapses which makes the two trains being pulled towards one another.

The coefficients for the different velocities can be seen in table 6.1.

Table 6.1: Coefficients from the meeting trains scenario.

Mean	C_D	C_S	C_L	C_{RM}	C_{PM}	C_{YM}
u_{67}	0.66360	0.05968	-0.09752	-0.02177	-1.52177	0.11707
u_{70}	0.65961	0.05966	-0.09954	-0.02059	-1.52515	0.09030
u_{73}	0.65758	0.05823	-0.09418	-0.02043	-1.51897	0.09519
Variance	C_D	C_S	C_L	C_{RM}	C_{PM}	C_{YM}
u_{67}	0.00657	0.06634	0.00649	0.00461	0.04679	0.48449
u_{70}	0.00650	0.07291	0.00675	0.00514	0.04103	0.49875
u_{73}	0.00634	0.07555	0.00668	0.00541	0.04170	0.50117

6.2 Train Exiting a Tunnel under Influence of a Wind Gust

Figure 6.14 show the train coming out of the tunnel at time step 0.6 s or position 42 m. The train is traveling in 70 m/s and the wind have a initial speed of 35 m/s. The train starts inside the tunnel and goes all the way out and past the wind gust.

In figure 6.15 the iso surfaces of low pressure are shown from the same position as seen in figure 6.14. The surfaces are colored by velocity W,i.e in z-direction. The red surfaces are wind going upwards and the blue are wind going downwards. The effect this has on the pressure of the train can be seen in the right picture where the relative pressure on the train body is shown.

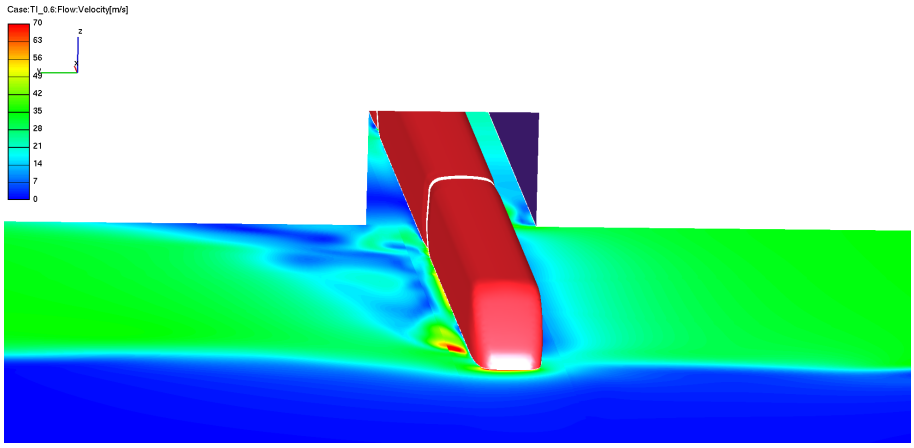

Figure 6.14: The wind gust hitting the train as it exists the train.

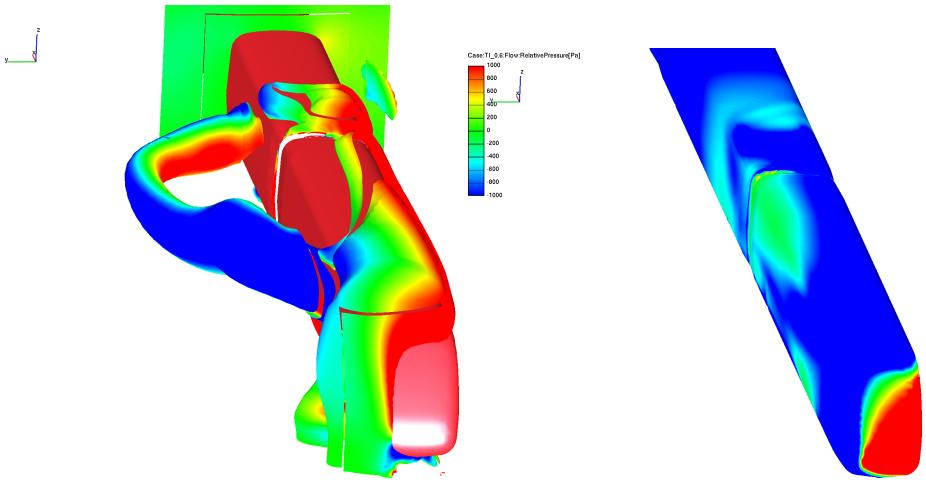

Figure 6.15: The low pressure surface around the train and the pressure on the train.

For the full scenario of pressure on the train one can study the time steps shown in figure 6.16. Note how the very low pressure on the top of the train travels as the train is exiting. This will cause a large lift force. Note also how the high pressure on the side travels from car to car. The magnitude of this pressure is however going down as the train travel, causing the side force to go down as well.

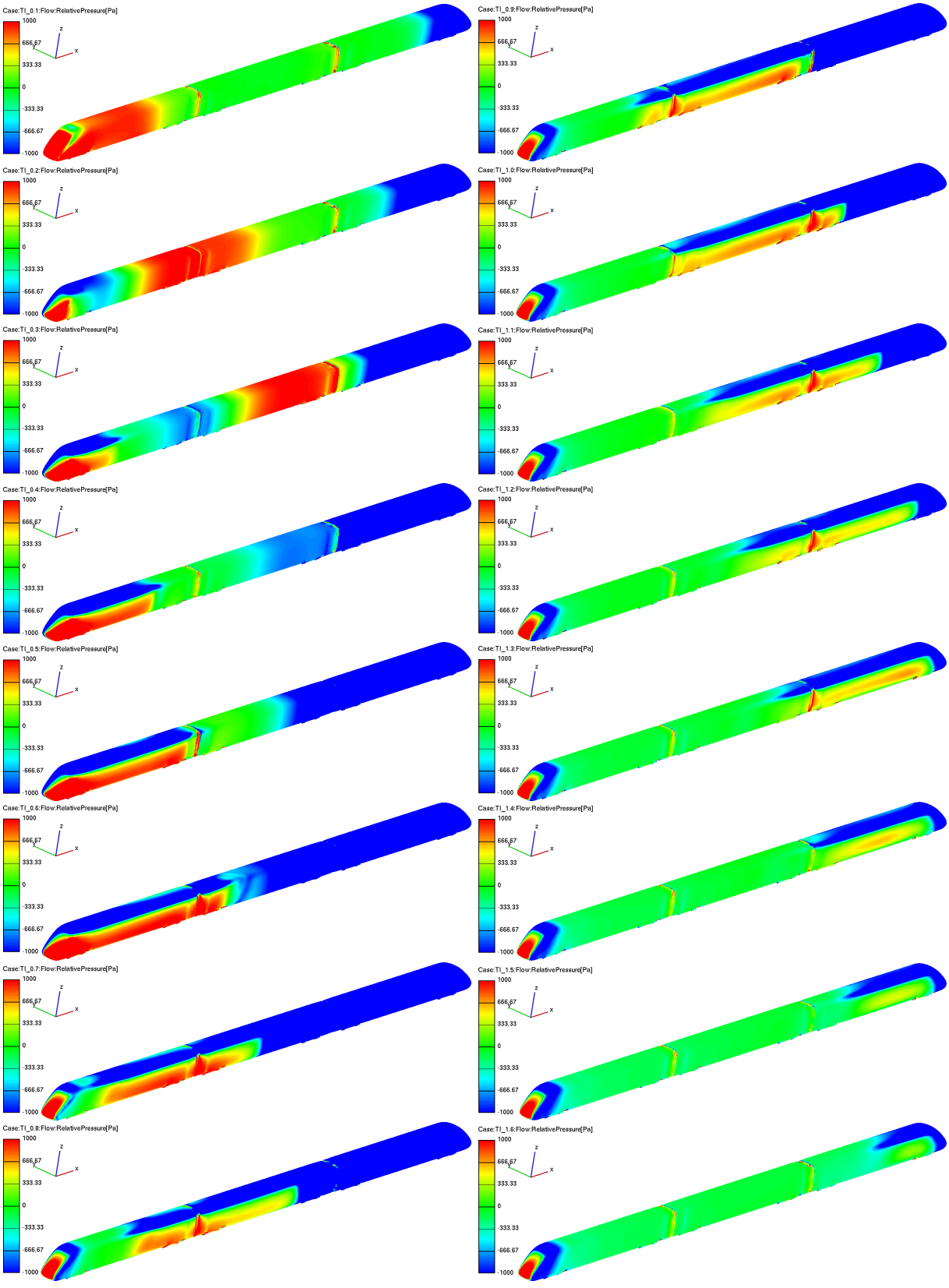

Figure 6.16: The relative pressure acting on the train during exit of tunnel.

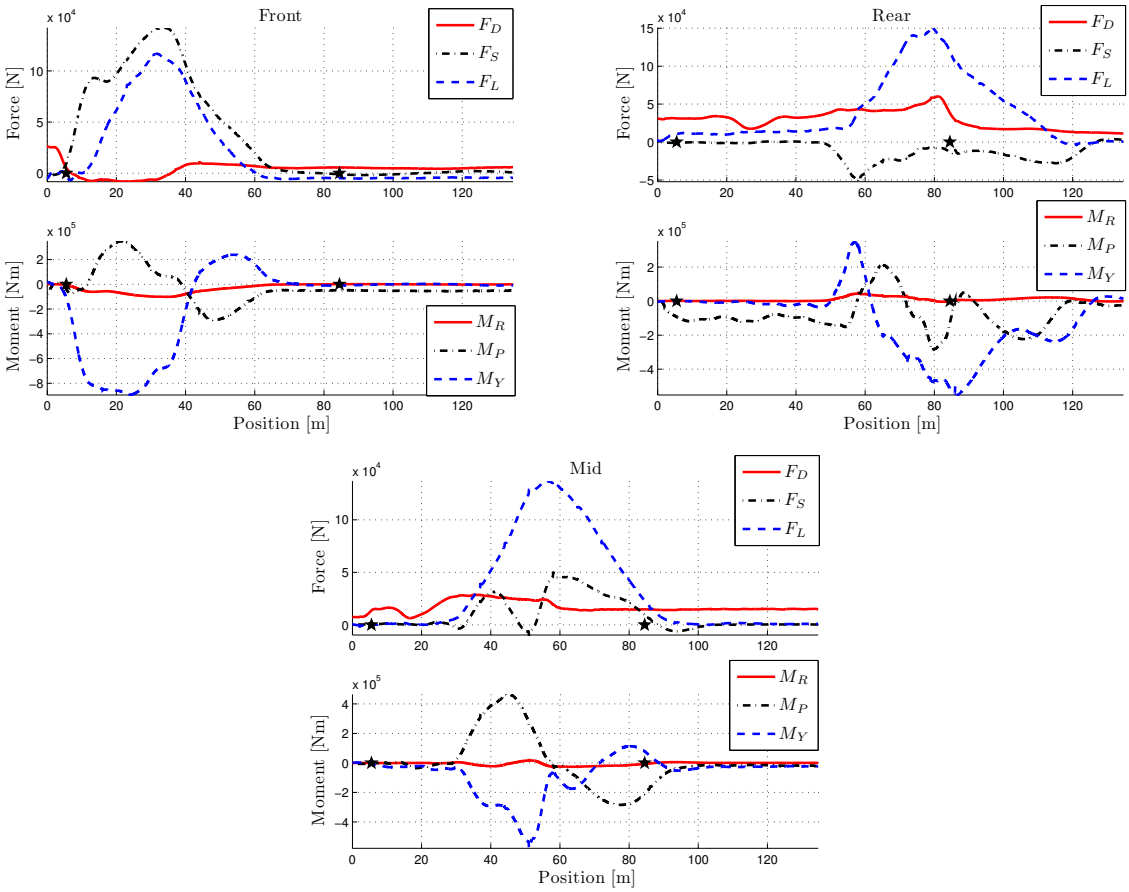

Figure 6.17: The forces and moments acting on the train cars.

The scenario was performed with the train traveling at 70 m/s and an inlet wind of 35 m/s at the first 30 m ($10W$) from the tunnel exit. This is meant to simulate a strong wind gust influencing the train when exiting the tunnel.

In figure 6.17 the forces and moments acting on the different cars can be seen. The stars mark when the nose of the train exit the tunnel and when the rear tail of the train exit the tunnel. The lift force is the greatest force acting on the train and can be seen wander from one car to the next during the exit of the tunnel.

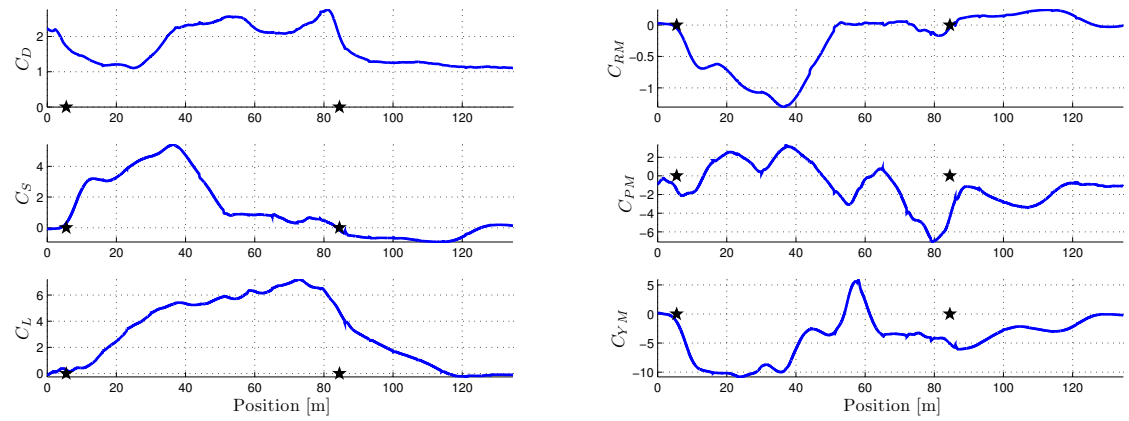

Figure 6.18: The force coefficients on the train from meeting a train at 140 m/s.

The coefficients were calculated for the whole train as in (2.18-2.19) and is seen in figure 6.18.

Table 6.2: Coefficients from the tunnel scenario.

Mean	C_D	C_S	C_L	C_{RM}	C_{PM}	C_{YM}
u_{70}	1.71200	1.15886	3.20398	-0.22480	-1.08609	-4.05955
Variance	C_D	C_S	C_L	C_{RM}	C_{PM}	C_{YM}
u_{70}	0.28743	3.63883	6.43379	0.21016	5.05362	13.40303

6.3 Discussion of CFD method and results

The difference in flows between the two cases is large. It is interesting to study two so different scenarios and what consequences they have on the stability and comfort. A similar simulation to a train leaving a tunnel has been done in [12], where the train exiting a tunnel is made with an entirely different method. The behaviour and magnitudes of the forces and moments are similar which indicate a reasonable result. The fact that the train geomtry used for CFD calculations is from ICE2 and that the data used in the dynamic calculations is from a different high speed train is also an issue for using the results. The differences in shape of nose and body will have influence of the results which have been studied in [6], but the differences will probably mainly consist of slight changes in magnitude of the forces.

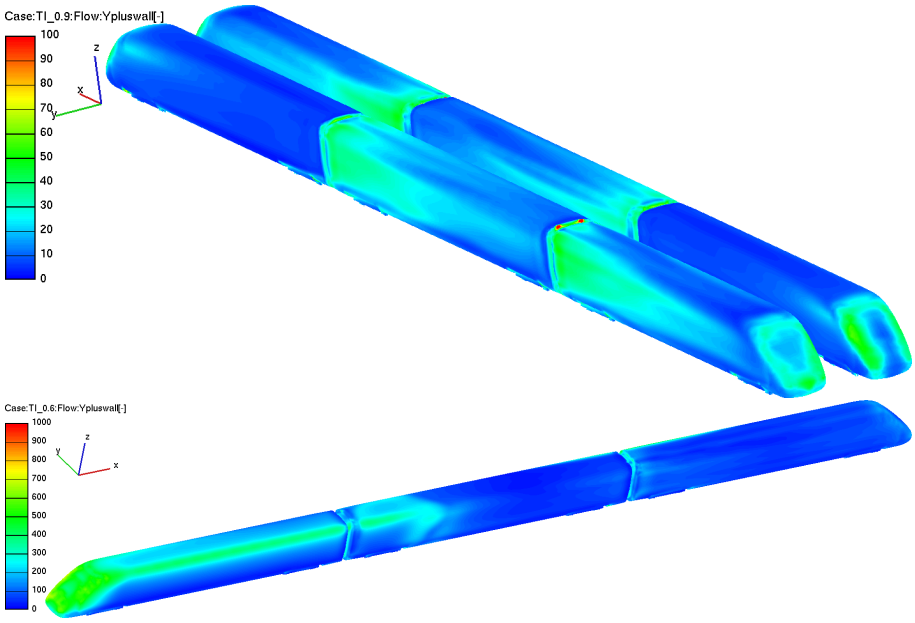

Figure 6.19: The y^+ on the walls of the trains.

The resolution of the cases can be seen in figure 6.19. The upper figure shows the y^+ of the trains passing each other. The value never passes 100 except at local positions where the velocity is locally high. The fact that the flow is resolved to this point means that the use of wall functions is applicable. For the train exiting the tunnel the value of y^+ exceed 600 on the front. The consequences of this is hard to predict but the results are probably good enough to use.

The Courant number (CFL number) is supposed to be below one at all times in the entire mesh to ensure that the information travels from one cell to the next. The Courant number can however locally be higher without affecting the flow. The Courant number at critical positions around the trains in both cases can be seen in figure 6.20. The Courant number is mostly below one in both cases. Both y^+ and CFL is supposed to be as low as possible to get more accurate results. These two contradict one another. Close to the walls

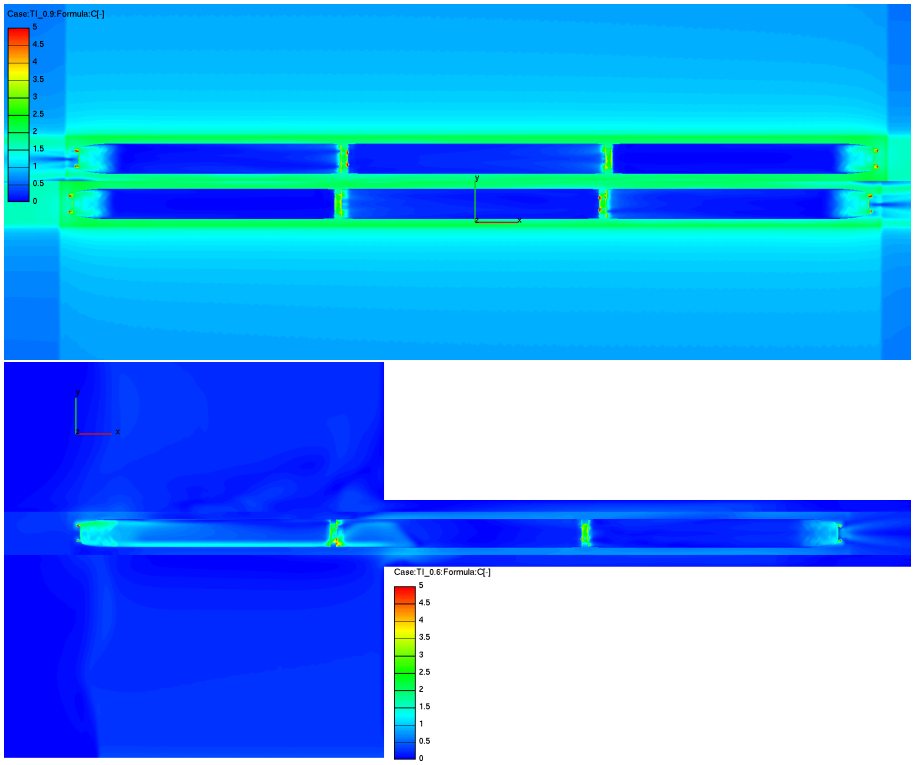

Figure 6.20: The Courant number on the walls around the trains.

where y^+ is calculated the Courant number is calculated for the same height, i.e. $y = h$ in (2.20) and (2.23). So having small cells to resolve the flow also means that the time step has to be lowered.

7 Results from Vibration Dynamic Simulations

Throughout all results all the cost functions should be minized, i.e. a lower J_c, $J_{s,1}$ and $J_{s,2}$ is better, where they meassure comfort and two stability measurements respectively. In the scenario with meeting trains, the flange never touches the rail, so $J_{s,1}$ is zero for all simulations.

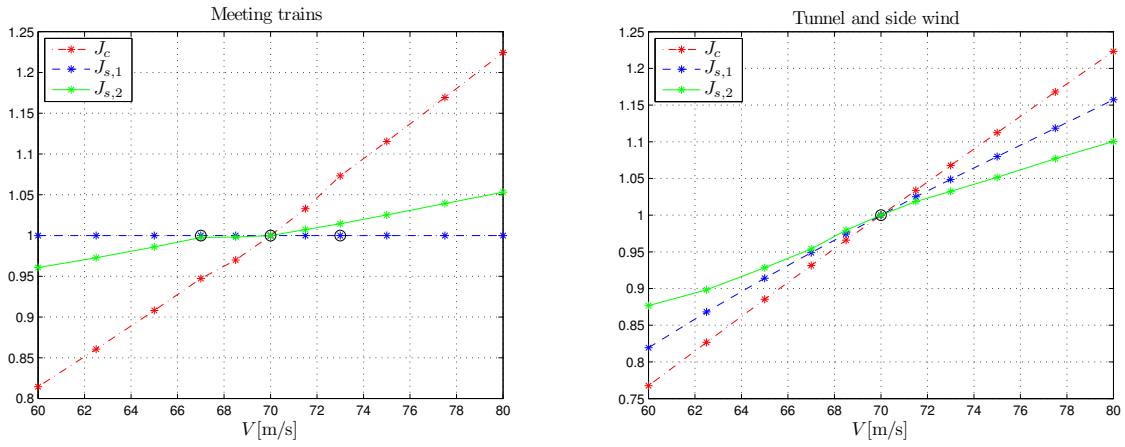

Figure 7.1: Comfort and stability measurements over speed with the initial spring and damper coefficients for a passive coupling.

Table 7.1: Absolute values of the stability and comfort measurements for both scenarios at 70 m/s.

	J_c [m/s^2]	$J_{s,1}$ [-]	$J_{s,2}$ [m]
Meeting trains	0.66	0.00	4×10^{-4}
Tunnel and side wind	10.71	0.55	245×10^{-4}

A speed sensitivity analysis was performed over a five second long simulation for both scenarios. Extrapolation for the higher and lower speeds was done as described in (3.19). In figure 7.1 the results for both scenarios are shown with the comfort and stability measurements normalized at 70 m/s. For the meeting trains, data was available for three speeds, which fit into the straight almost linear increase well, but for the train leaving the tunnel data was only available for 70 m/s and to achieve true air speed the side wind should also be considered scaled when extrapolating the forces.

It is interesting to note that the comfort and stability measurements scale linearly, while in fact the forces on the train, both wind loads and rail contact behaviour does not. A comparison between the scenarios can be seen in table 7.1. The side wind causes many times higher load on the train, and it also causes the flange to hit the rail.

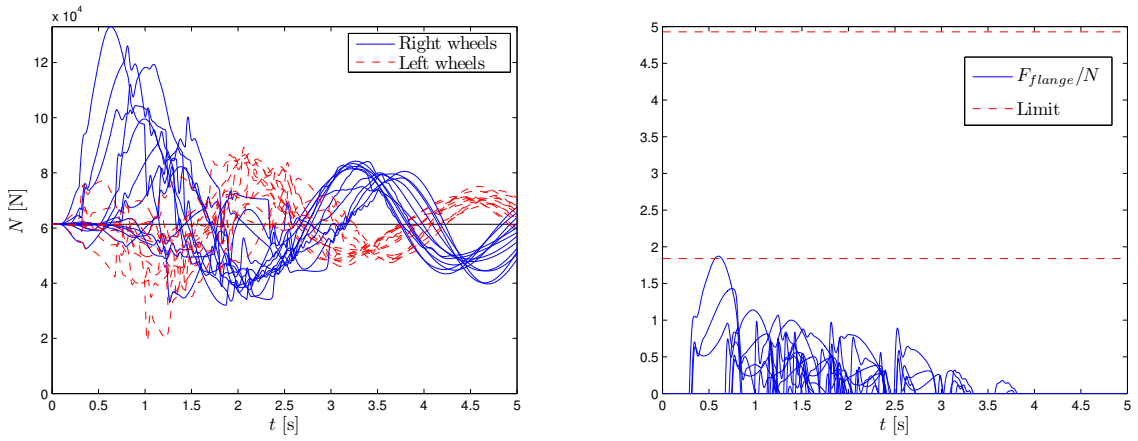

Figure 7.2: Normal forces and flange forces on the wheel-rail contact for the train for the tunnel scenario.

It is not easy to compare the measurements, but in the tunnel and side wind, $J_{s,1} = 0.55$ is very high, with high risk of derailment. The normal forces and flange forces using the optimized parameters in table 7.2 are shown in figure 7.2. For the normal forces one can see that the train nearly lifts and for the flange forces are already to high, i.e. risk of wheel climbing. The limits shown in figure 7.2 are for when the wheel is rolling towards or from the rail.

7.1 Optimization of the Coupling

The two different scenarios gives two very different optimization criteria as seen in figure 7.3 and figure 7.5. For meeting trains, it's typically better with higher values, and for the tunnel the lower is better. When looking at c_{roll} the spectrum was unnecessarily large, and for both scenarios a optimum value can be found at the very beginning in figure 7.4 and 7.6. In table 7.2 some values chosen as optimal is compared and they were intentionally picked as similar as possible for both scenarios.

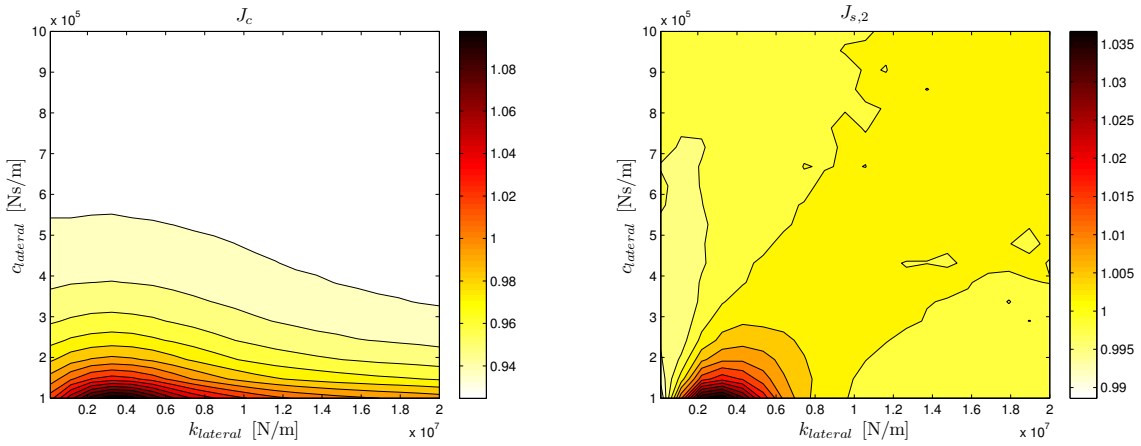

Figure 7.3: Optimization of the lateral spring and damper for meeting trains.

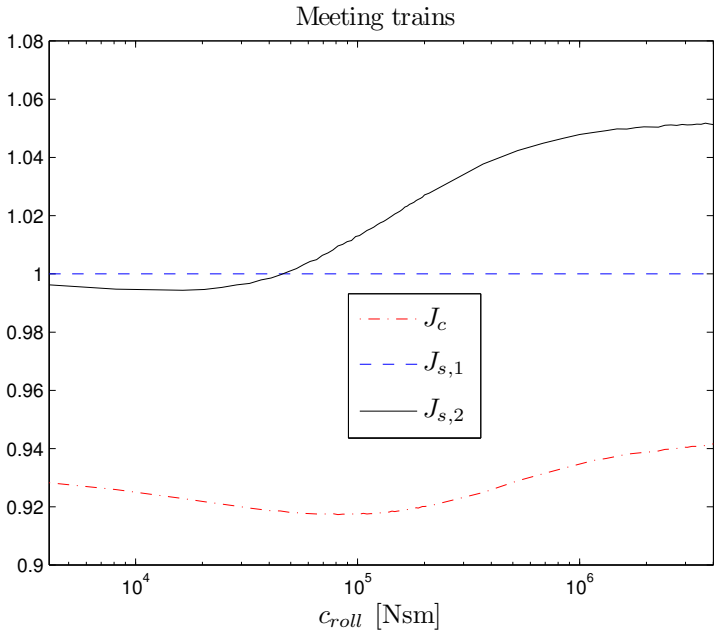

Figure 7.4: Optimization of the roll damper for meeting trains.

Table 7.2: Comparison of the optimized values.

	Initial	Meeting trains	Tunnel and side win
$k_{lateral}$ [kN/m]	2×10^4	50	50
$c_{lateral}$ [kNs/m]	100	700	100
c_{roll} [kNsm]	5	20	20
Relative change of J_c		-7.82%	-7.18%
Relative change of $J_{s,1}$			-4.58%
Relative change of $J_{s,2}$		-0.55%	-8.88%
Effect in speed		-3 to -4[m/s]	-3 to -5[m/s]

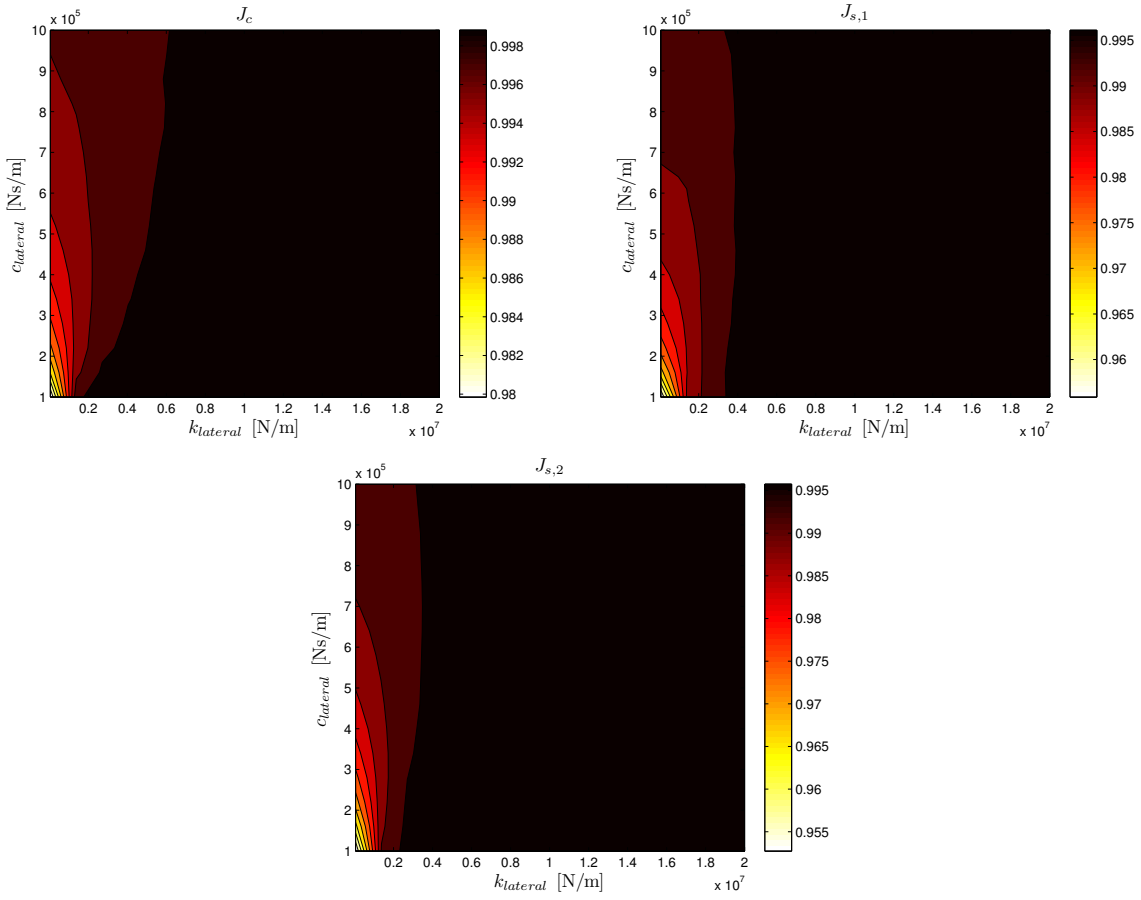

Figure 7.5: Optimization of the lateral spring and damper for tunnel and side wind.

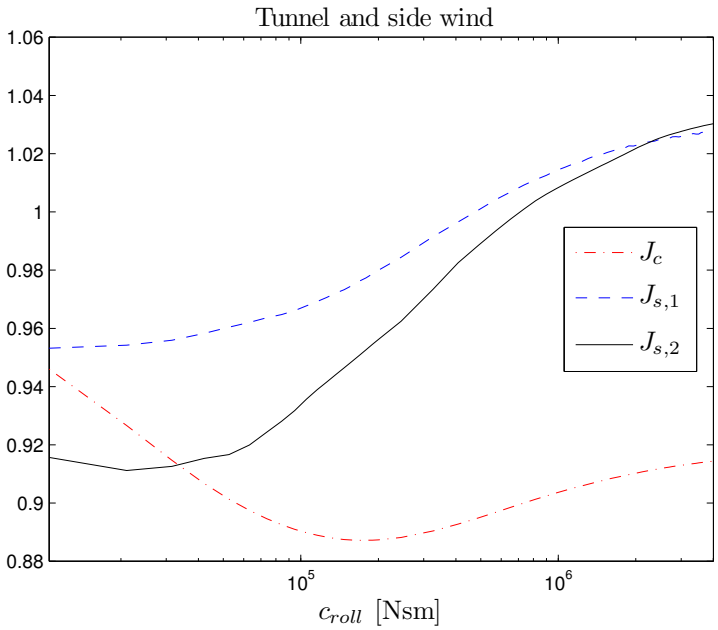

Figure 7.6: Optimization of the roll damper for tunnel and side wind.

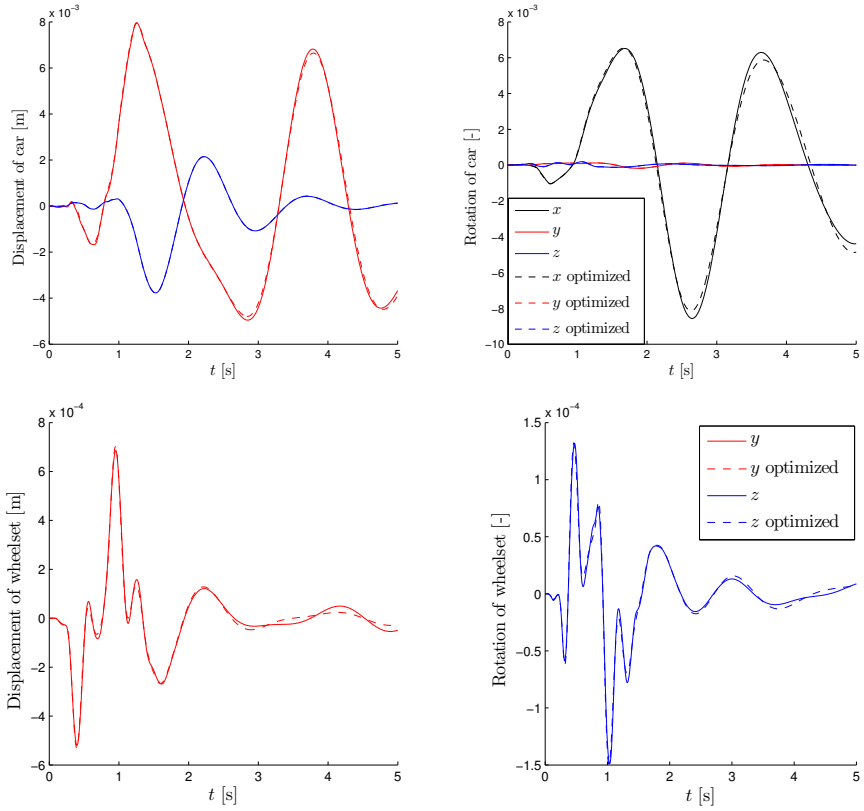

Figure 7.7: The trains displacement for the meeting trains.

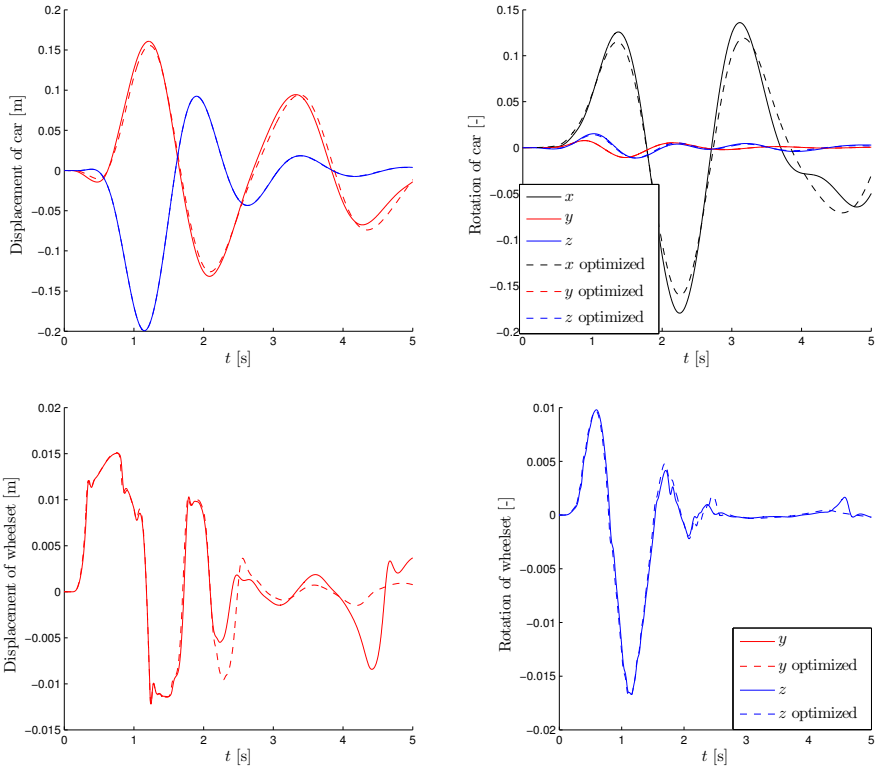

Figure 7.8: The trains displacement for the tunnel and side wind.

Figure 7.7 and 7.8 shows how the middle train car and the front wheelset on the middle car responds in each respective scenario.

7.2 Coupling Sky-hook

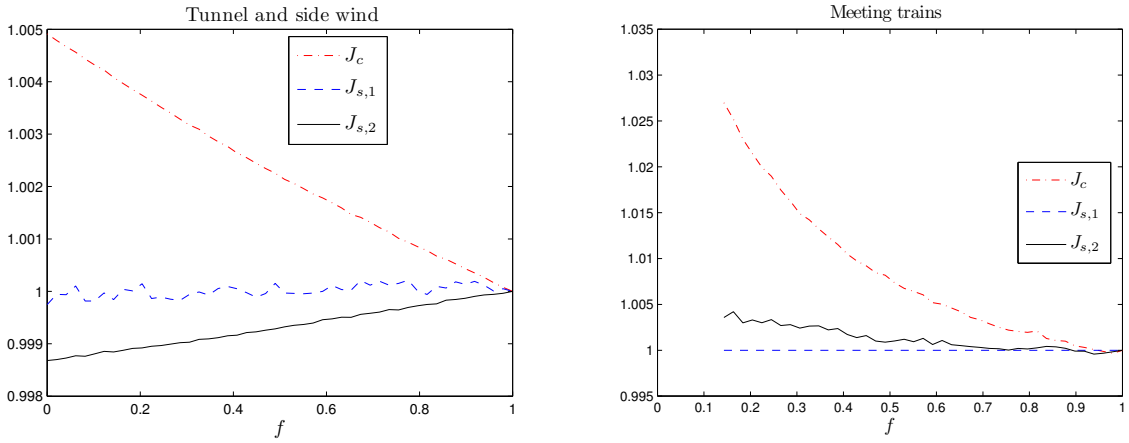

Figure 7.9: Sky-Hook for varying fractions.

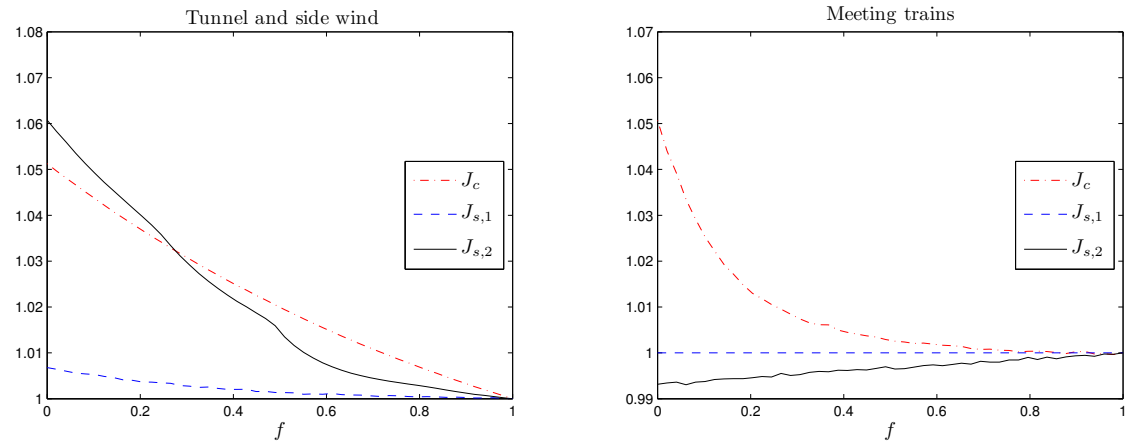

Figure 7.10: Ground-Hook for varying fractions.

By sky-hook in these simulations the sky is referred to as the locomotives, and the middle car the ground. If $v_{sky}\Delta v > 0$ then just a fraction, f, of the damping coefficient is used, i.e. $c_{y,min} = fc_y$ and $c_{roll,min} = fc_{roll}$. For the sky-hook on the meeting trains the ODE solver had problems, thus the values are missing.

8 Conclusions

Only a few simplifications were done on the model as a whole which are described and motivated in the theory for this report. The implementation in MATLAB used high level mathematics and automated construction to minimize the amount of manual work. The contact model was built upon established techniques for contact, creep and forces. The components of the system have been tested individual and the dynamic simulations are very trustworthy.

The scenario with the meeting trains will only cause slight vibrations for the passengers, while the tunnel and side wind has a major impact on the stability of the train. For the side wind at 35 m/s the train would experience to much movement, and at these weather conditions (12 on the Beaufort scale) the train cannot go at full speed due to

safety concerns. Such wind can make large objects airborn and these conditions occur a few times a year around Europe.

One of the most interesting results is how very linearly the stability and comfort measurements scale towards the true air speed. The CFD simulations only cover a spectrum between 67 to 73 m/s in the meeting trains scenario, and only for 70m/s for the tunnel, but the loads on the train behaves very similarly between 67 and 73m/s making it reasonable to scale using constant drag and lift coefficients. Even if the flow starts to behave differently when nearing 60 and 80 m/s, the speed analysis still show that the comfort and stability still change linearly for a quadratically changing wind load and highly nonlinear reaction forces from the wheel contact.

The swaying movement of the train car in both scenarios can most likely be damped efficiently by the secondary suspension and most research on train dynamics focus on just the bogie. This work shows that there is also a noteable room for improvements in the coupling between the car bodies. While the initial parameters for the coupling were not accurately calibrated after an actual high speed train, the simulations show that carefully adjusting the coupling is important and can make a difference that equals the effect of lowering the speed around 3 m/s $\approx$ 10 km/h. The initial coupling parameters only model a simple, stiff connection with some small internal damping and the real coupling might already have better or worse behaviour. In particular the effects from changing the roll damper are very strong for smaller values, making it unreasonable to believe that a optimized coupling is already in place, unless a similar analysis have been performed. Lowering the lateral stiffness by designing a momentless joint in the coupling might be a good idea, but more scenarios needs to be studied.

9 Recommendations

For further work we recommend the following:

- Improve mesh for movement. Some information is lost when the mesh is moved far from the initial position. The mesh quality could also be improved, the automatic mesh generator does not create a perfect mesh.
- It is difficult to use a moving mesh. Much control is lost. They are time consuming and when a calculation is started it is difficult to alter the settings.
- More velocity tests is needed. The velocities of the meeting trains should be done at several more velocities as well as the velocity of the train and the wind speed for the tunnel scenario. More is always good for use in the dynamic calculations.
- Cases with side wind velocity should be lowered. The 35 m/s currently used is a worst case scenario. To improve dynamic calculations and optimization of trains lower wind velocities should be used.
- Look at PID regulators in the coupling.
- Compare the performance of active damping in the secondary suspension to the coupling.
- Compare stability and comfort measurements with non wind related scenarios such as curves.
- The other springs and dampers could also be put under optimization, especially the roll spring.

References

[1] Fire v2008 cfd solver manual, 2008.

[2] Matlab manual for ode solvers. http://www.mathworks.com/access/helpdesk/help/techdoc/ref/ode45.html, 2008.

[3] Branislav Basara. An eddy viscosity transport model based on elliptic relaxation approach. *AIAA J.*, 44:1686–1690, 2006.

[4] Bengt Sundström et al. *Handbok och formelsamling i Hållfasthetslära*. Fingraf AB, Södertälje, Sweden, 2005.

[5] Bo Jonsson et al. *Höga hastigheter i SJ persontrafik*. SJ Centralförvaltning, Stockholm, Sweden, 1969.

[6] Erik Bjerklund et al. *Design of High-Speed Trains for Cross-Wing Stability*. Chalmers Tekniska Högskola, 2007.

[7] Evert Andersson et al. *Rail Vehicle Dynamics*. Universitetsservice AB, Stockholm, Sweden, 2007.

[8] Kemal Hanjalic et al. A robust near-wall elliptic-relaxation eddy-viscosity turbulence model for cfd. *International Journal of Heat and Fluid Flow*, 25:1047–1051, 2004.

[9] Arieh Iserles. *A First Course in the Numerical Analysis of Differential Equations*. Cambridge University Press, 2004.

[10] Carsten Nordstrøm Jensen and Hans True. Application of a wheel-rail contact model to railway dynamics in small radius curved tracks. *Nonlinear Dynamics*, 13:117–129, 1997.

[11] K.L. Johnson. *Contact Mechanics*. Cambridge University Press, 1985.

[12] Siniša Krajnović. Computer simulation of a train exiting a tunnel through a varying crosswind. *International Journal of Railway*, 3:99–105, 2008.

[13] João C. Pombo and Jorge A.C. Ambrósio. Application of a wheel-rail contact model to railway dynamics in small radius curved tracks. *Multibody Syst Dyn*, 19:91–114, 2008.

[14] M. Popovac and K. Hanjalic. Compound wall treatment for rans computation of complex turbulent flows and heat transfer. *Turbulence and Combustion*, 78:177–202, 2007.